A 3500-year tree-ring record of annual precipitation on the north-eastern Tibetan Plateau

Bao Yang[a,1], Chun Qin[a], Jianglin Wang[a], Minhui He[a], Thomas M. Melvin[b], Timothy J. Osborn[b] and Keith R. Briffa[b]

[a]Key Laboratory of Desert and Desertification, Cold and Arid Regions Environmental and Engineering Research Institute, Chinese Academy of Sciences, Lanzhou, Gansu Province, China

[b]Climatic Research Unit, School of Environmental Sciences, University of East Anglia, Norwich, NR4 7TJ, UK

[1]E-mail: yangbao@lzb.ac.cn

Supplementary Information

Section A: raw tree-ring and climate data

Section B: chronology construction

Section C: chronology presentation and comparison

Section D: chronology calibration

Section E: interpretation of the variability in QLS inferred precipitation

Section F: exploring and quantifying QLS chronology uncertainty

Section G: comparison of QLS inferred precipitation and various temperature reconstructions

SI Section A: raw tree-ring and climate data

Table SA1. Details of the Qilian Juniper ring-width data groups used in this study.
The full dataset comprises four larger regional subsets (DLH, DL, HYG, ZMS) containing data located at 21 individual sampling sites. The HYG and ZMS data make up the 'Northern' and the DLH and DL data make up the 'Southern' chronologies (see Figures SF2, SF4 and SF5). The detailed information includes region, site, latitude, longitude, elevation, chronology period (Length), Mean tree age (MSL), Mean sensitivity (MS), First order autocorrelation (AC1), start and end dates of the chronology with sample replication >6 trees (Start/End >6). DLH = Delingha, DL = Dulan; HYG = Haiyagou, ZMS = Zhamashi. The symbol * indicates data from archaeological contexts. The chin005 and chin006 datasets were acquired from the International Tree-Ring Data Bank (ITRDB) held at the World Data Center for Paleoclimatology. We also used some data from the Dulan archaeological chronology (named DL) derived from ref.14 in the main text. All site locations are shown in Figure 1.

Region	Site	Latitude (°N)	Longitude (°E)	Elevation (m)	Length	MSL	MS	AC1	Start>6	End>6
Delingha (DLH)	ZHG	37.5	97.15	3814-4175	4649	596	0.31	0.73	-2062	2011
	SBP	37.47	97.25	3851-4100						
	MNT	37.45	97.68	3740-4012						
	YMT	37.45	97.63	3743-3804						
	GMP*	37.42	97.78	3251-3312						
	HMP*	37.4	97.58	3390-3411						
	NMP*	37.33	97.65	3193-3216						
	QMP*	37.43	97.78	3301-3349						
	SG	37.28	98.43	3677-4048						
	HTP	37.03	98.65	3702-3933						
Dulan (DL)	ND	36.33	98.7	3617-3904	1853	392	0.38	0.60	876	2011
	XRD	35.98	98.12	3770-3906						
	XRH	35.45	98.2	3768-4040						
	Chin005	37	98.5	3800						
	Chin006	36	98 °E	3800						
Haiyagou (HYG)	HYG	38.7	99.70	2863-3517	1954	587	0.27	0.80	368	2009
	HMG	38.43	99.97	3443-3493						
	XBG	38.42	99.88	3062-3348						
Zhamashi (ZMS)	BG	38.15	99.88	3300-3500	1578	649	0.28	0.80	450	2009
	YHL	38.25	99.78	3255-3574						
	ZMSX	38.15	99.95	3314-3491						
ALL	-	-	-	**2863-4175**	**4649**	**592**	**0.30**	**0.75**	**-2062**	**2011**

Table SA2. Some basic statistics for sub-groups of indices, here created by standardising with a 30-year high-pass spline.

Corr - the mean correlation of each index series with the chronology (excluding that series).
Rbar - the mean inter tree correlation.
MnRaw - the mean value of TRW measurements for the group.

All raw measurement data, cross correlation tables, chronologies and reconstructed precipitation data along with their confidence intervals are available at
http://www.cru.uea.ac.uk/cru/papers/yang2013pnas/

File name	Trees	Start	End	Years	Rings	Corr	RBar	MnRaw
chin005	59	840	1993	1154	50162	0.80	0.65	0.31
chin006	60	159	1993	1835	41405	0.73	0.56	0.30
dulan	157	933	2011	1079	60366	0.70	0.51	0.36
GM	174	-1495	1243	2739	94060	0.65	0.44	0.21
HYG	69	56	2009	1954	44953	0.59	0.36	0.33
ZMSX	91	432	2008	1577	63460	0.62	0.40	0.29
DLH	593	-2637	2011	4649	437862	0.67	0.45	0.30
All sites	1203	-2637	2011	4649	792268	0.62	0.38	0.30

Table SA3. Site locations and meta data for metreorological stations used in this analysis. Records of mean monthly temperature and monthly precipitation data were obtained from six national meteorological stations located nearest to the tree growth sites. See Fig. 1 for site locations.

Station name	Coordinates (latitudes, longitudes)	Altitude (m)	Period
Delingha	37.37 ºN, 97.37 ºE	2981	1956-2012
Dulan	36.30 ºN, 98.10 ºE	3191	1954-2009
Chaka	36.78 ºN, 99.08 ºE	3088	1956-2000
Qilian	38.18 ºN, 100.25 ºE	2787	1957-2012
Tuole	38.75 ºN, 99.33 ºE	2770	1957-2011
Yeniugou	38.42 ºN, 99.58 ºE	3320	1960-2012

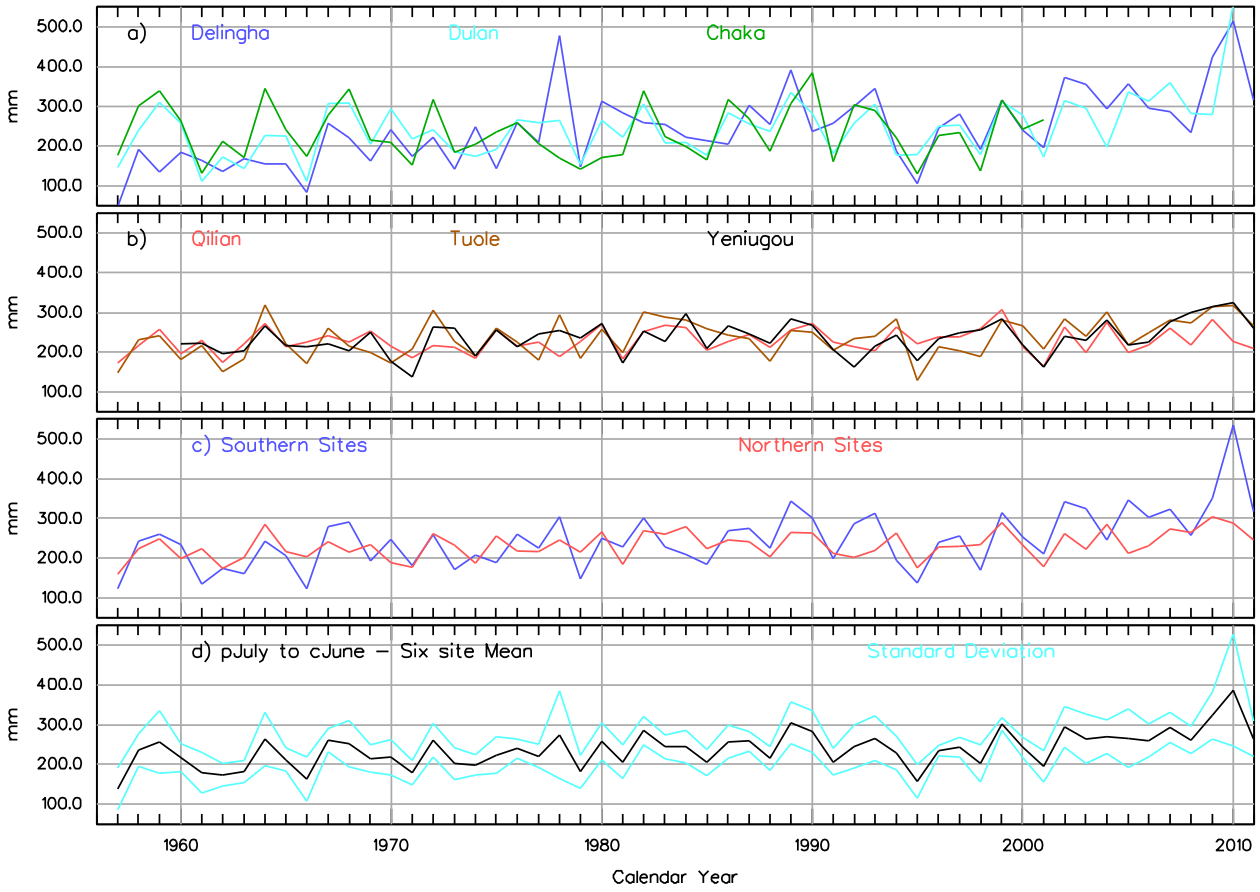

Fig. SA1. Mean annual (previous July to current June) precipitation (in mm) for the period 1957 to 2011 at six meteorological stations representing the study region (see Fig. 1). For each station, the mean value of each month's data was rescaled to be equal to the mean value of data for that month from all six stations (the regional data for that month) using only those years that are common to all six sites. The twelve monthly values for each site were averaged to produce annual means for a) the stations corresponding to the "southern" sites chronology (Delingha, Dulan and Chaka) and b) the "northern" sites (Qilian, Tuole and Yeniugou). Fig. c) shows the means of the rescaled values for the northern (red) and southern (blue) sites, and d) shows the means of all six sites (black) along with bands showing +/- 1.0 standard deviation (cyan) for each year. This all-site mean annual series was used as the predictand precipitation data against which the QLS chronology was rescaled to produce the reconstruction.

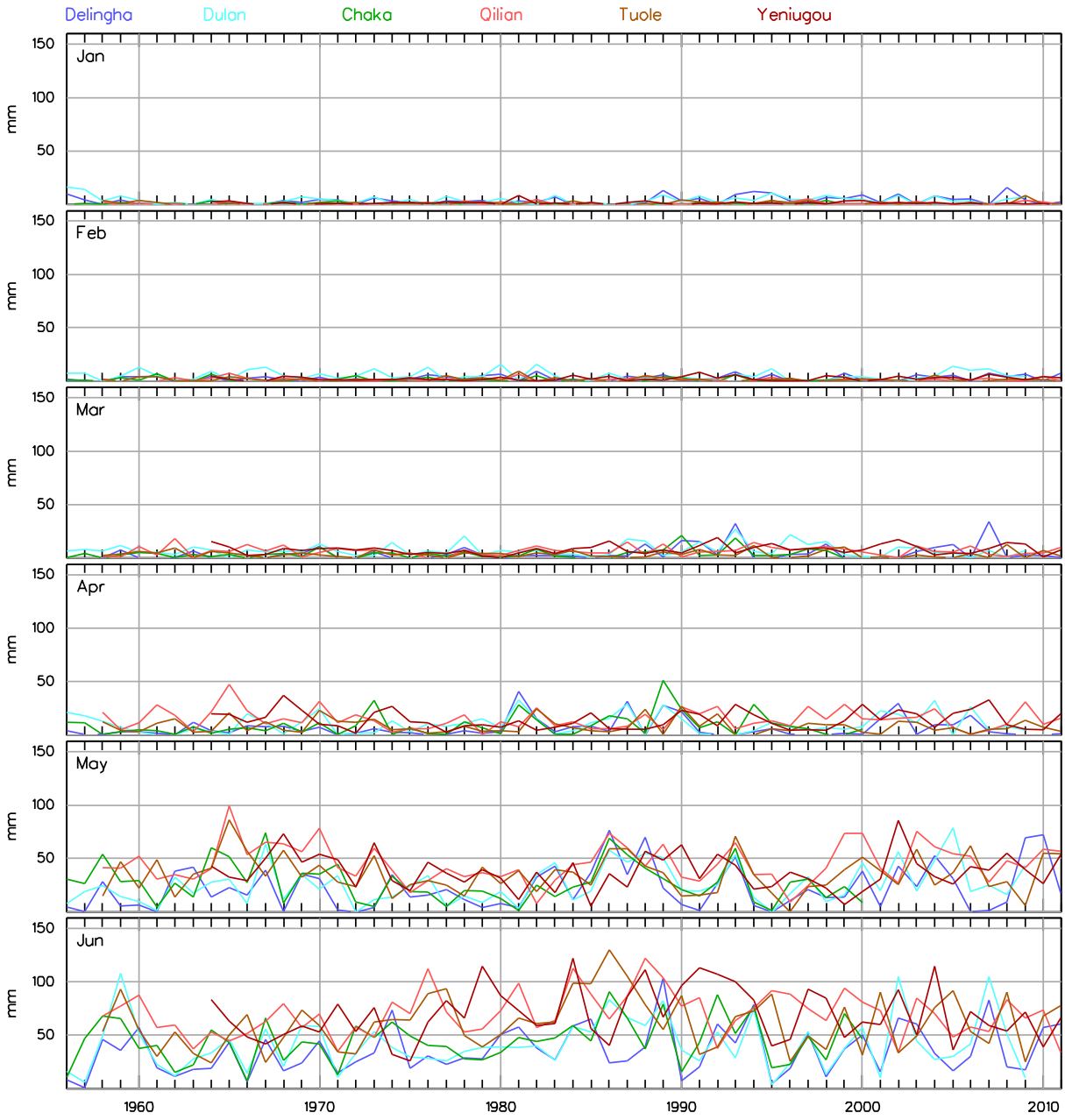

Fig. SA2. Monthly precipitation for each month January to December (in mm) for the period 1957 to 2011 for six meteorological stations; Delingha, Dulan, Chaka, Qilian, Tuola and Yeniugou.

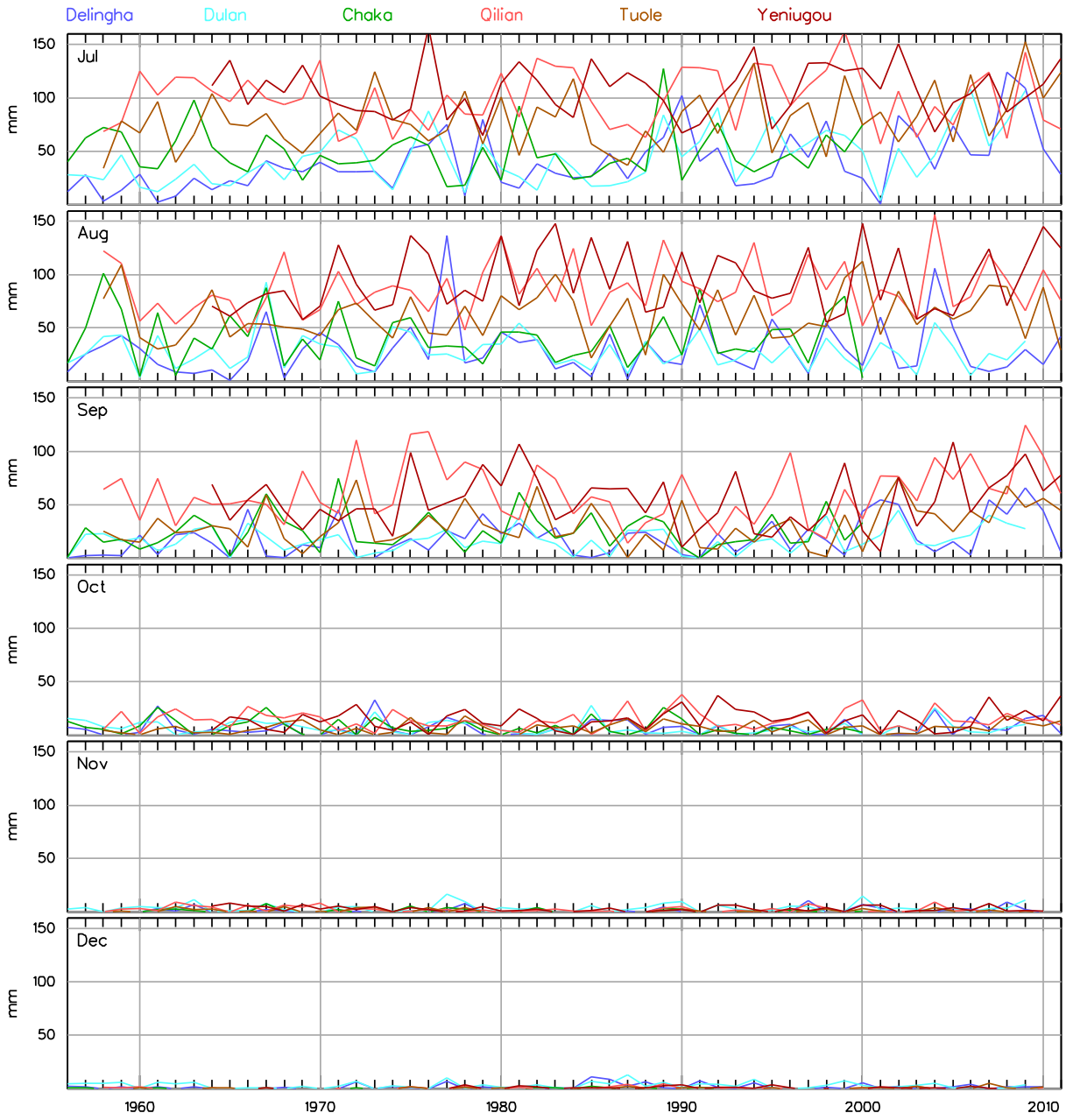

Fig. SA2. continued.

Fig. SA3. View of an old-aged Juniper in the arid environment of the north-eastern Tibetan Plateau.

Fig. SA4. Another view of typical "old age" Junipers.

Fig. SA5. A cross section of tree MNP312. The measurement tracks can be seen as polished areas.

Fig. SA6. A cross section of tree MNP357.

SI Section B: chronology construction

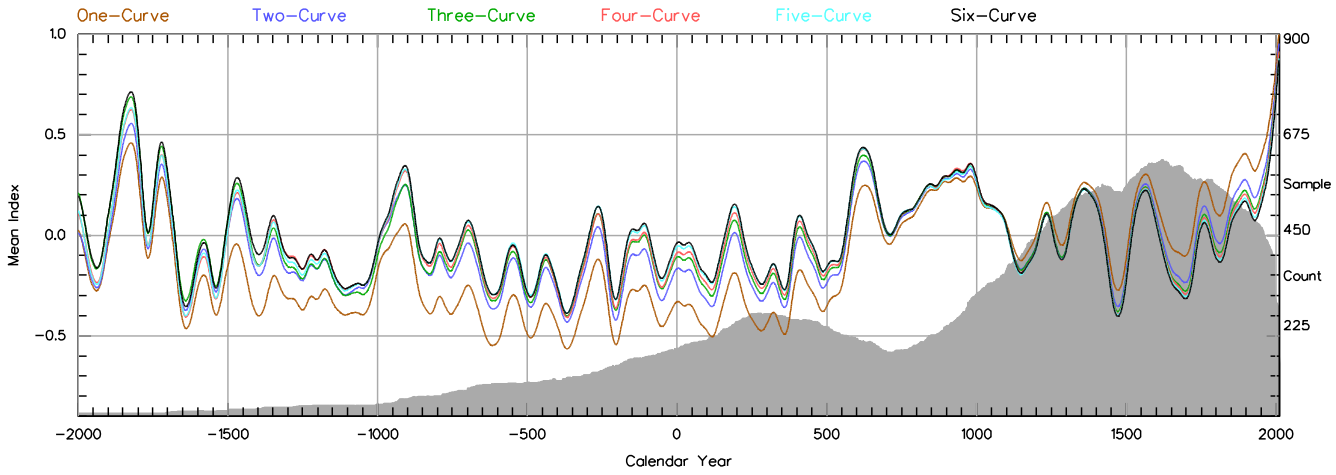

Fig. SB1. A comparison of six chronologies, all created using the same data from all the QLS trees, but standardised using from one to six RCS curves. All chronologies were produced using SF RCS with tree indices converted to have a normal distribution. Note that the version produced using one-curve SF RCS (brown) is not preferred because it exaggerates the overall trend in the series. This is because using a single RCS curve is not appropriate where the data from different regions have different overall mean growth rates under the "same" climate or where the total data set includes trees that grew in parallel but in different mean climates (though they may still show similar variability about the mean).

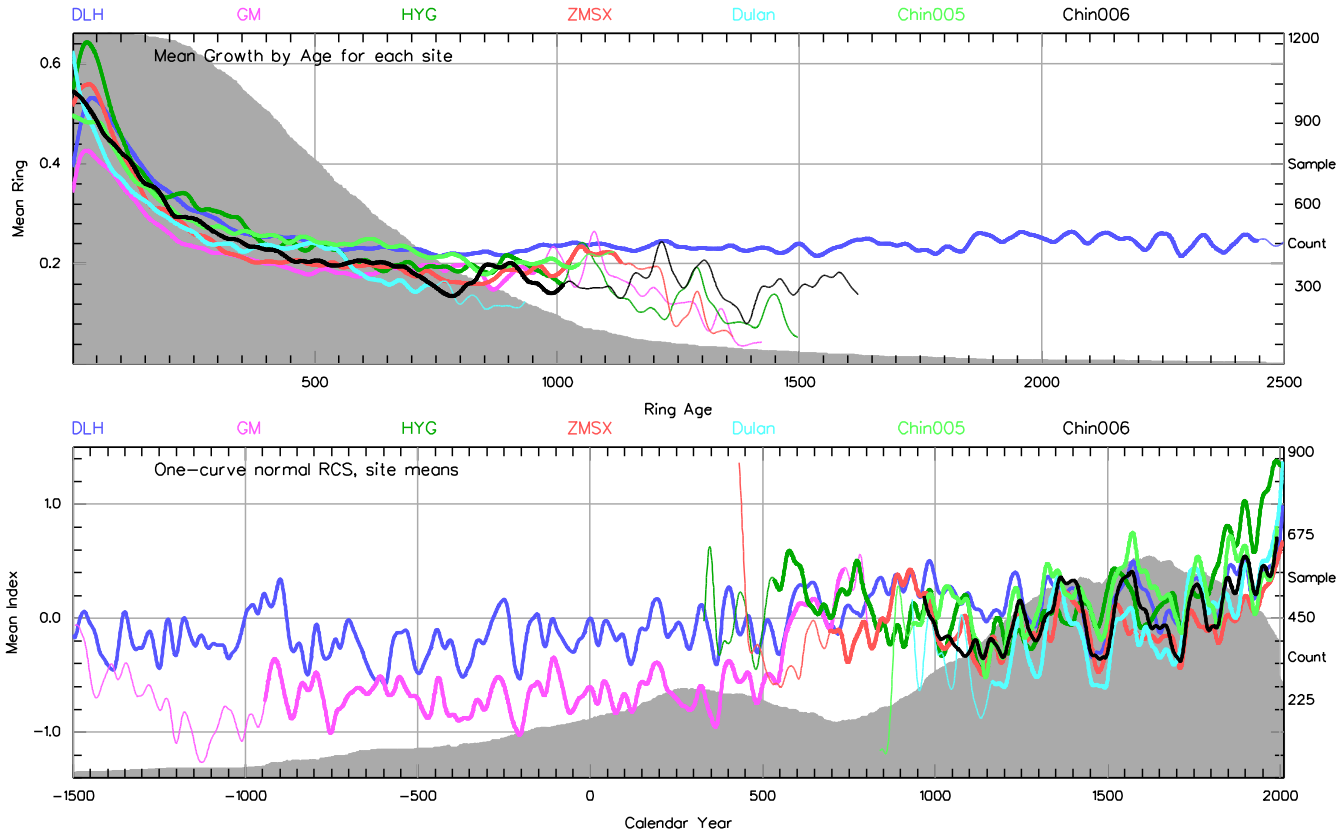

Fig. SB2. The upper panel shows plots of the mean ring width by ring age at each of the larger sub-sites in the QLS data set: DLH, GM, HYG, ZMSX, Dulan, Chin005 and Chin006 (see Table SA1). The GM data (archaeological material from tombs) has a lower mean growth rate than all the other sites. Here all the data have been combined and standardised with one-curve normal SF RCS and chronologies of the means of tree indices over time for each site are plotted in the lower panel to demonstrate potential bias involved in using only a single RCS curve to standardise all data. The archaeological data from the GM site are generally from slower growing trees and shows substantially lower indices prior to 600 CE than the indices of the DLH site. We presume these trees grew on sites at lower elevations with lower mean precipitation levels. Chronologies and mean ring-width curves have been smoothed with a 50-year spline. Note that these (mean growth by age) curves are not those used to produce the chronology. The SF RCS curves used to standardise the measurement data are produced by applying an age-dependent smoothing spline (1) to the measurements which produces a smoother curve than those shown here. Thin lines represent poorly replicated sections of the curves with less than 6 trees. The grey shading shows the sample (tree) replication.

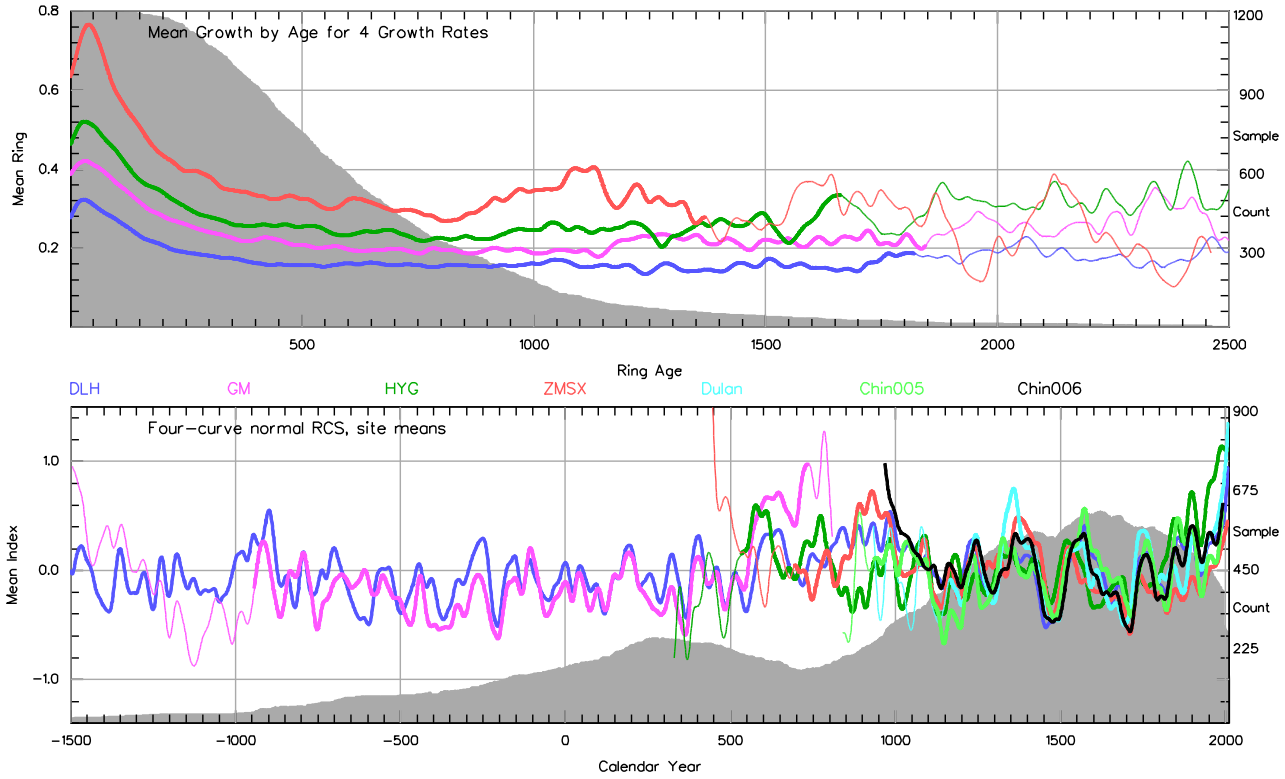

Fig. SB3. The combined measurement data for the QLS sub-sites (DLH, GM, HYG, ZMSX, Dulan, Chin005 and Chin006) were standardised with four-curve SF RCS with tree-indices converted to have a normal distribution. The upper panel shows the mean ring widths plotted by ring age for each growth rate from highest (red) to lowest (blue). Six site chronologies were created by separately averaging the indices of trees from each sub-site. The chronologies for each site sub-group are shown in the lower panel. The GM sub-chronology shows indices which are similar to those of the DLH site prior to 600 CE but appears to show a somewhat exaggerated step by comparison with the other series after this time. Chronologies and mean ring-width curves have been smoothed with a 50-year spline. Thin lines represent poorly replicated sections of the curves (with less than 6 trees). The grey shading shows the sample (tree) replication.

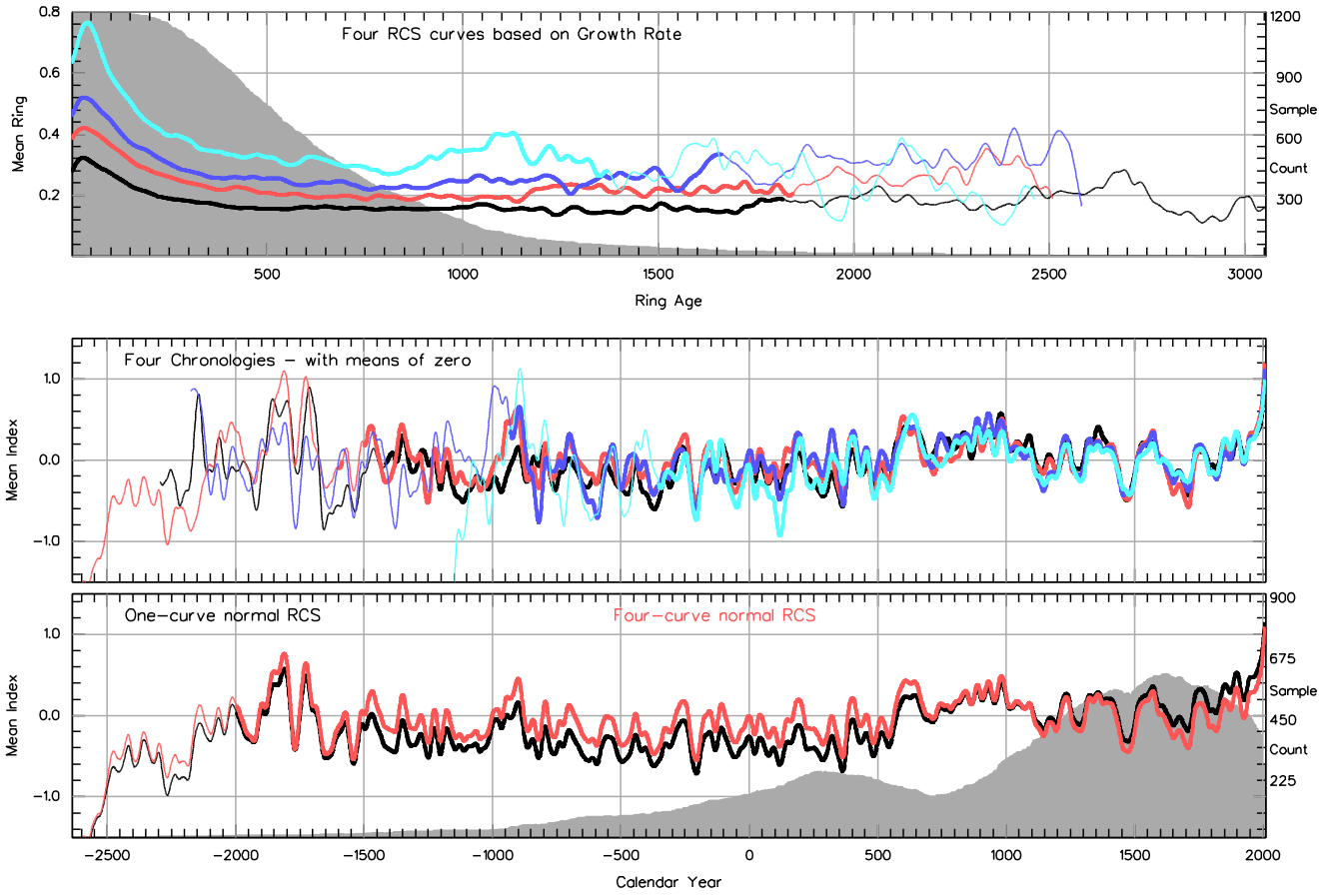

Fig. SB4. The combined data for the QLS sub-sites (DLH, GM, HYG, ZMSX, Dulan, Chin005 and Chin006) were standardised first using one-curve and secondly using four-curve normal SF RCS with tree indices converted to have a normal distribution. Four sub-chronologies, each comprising the tree-indices for one growth rate class (as produced by the four-curve standardisation with their means of approximately zero) are plotted in the middle panel (see Fig. 2 of main text). The lower panel compares chronologies created using one-curve and four-curve standardisation. Chronologies and mean ring-width curves have been smoothed with a 50-year spline. Thin lines represent poorly replicated sections of the curves with less than 6 trees. The grey shading shows the sample (tree) replication.

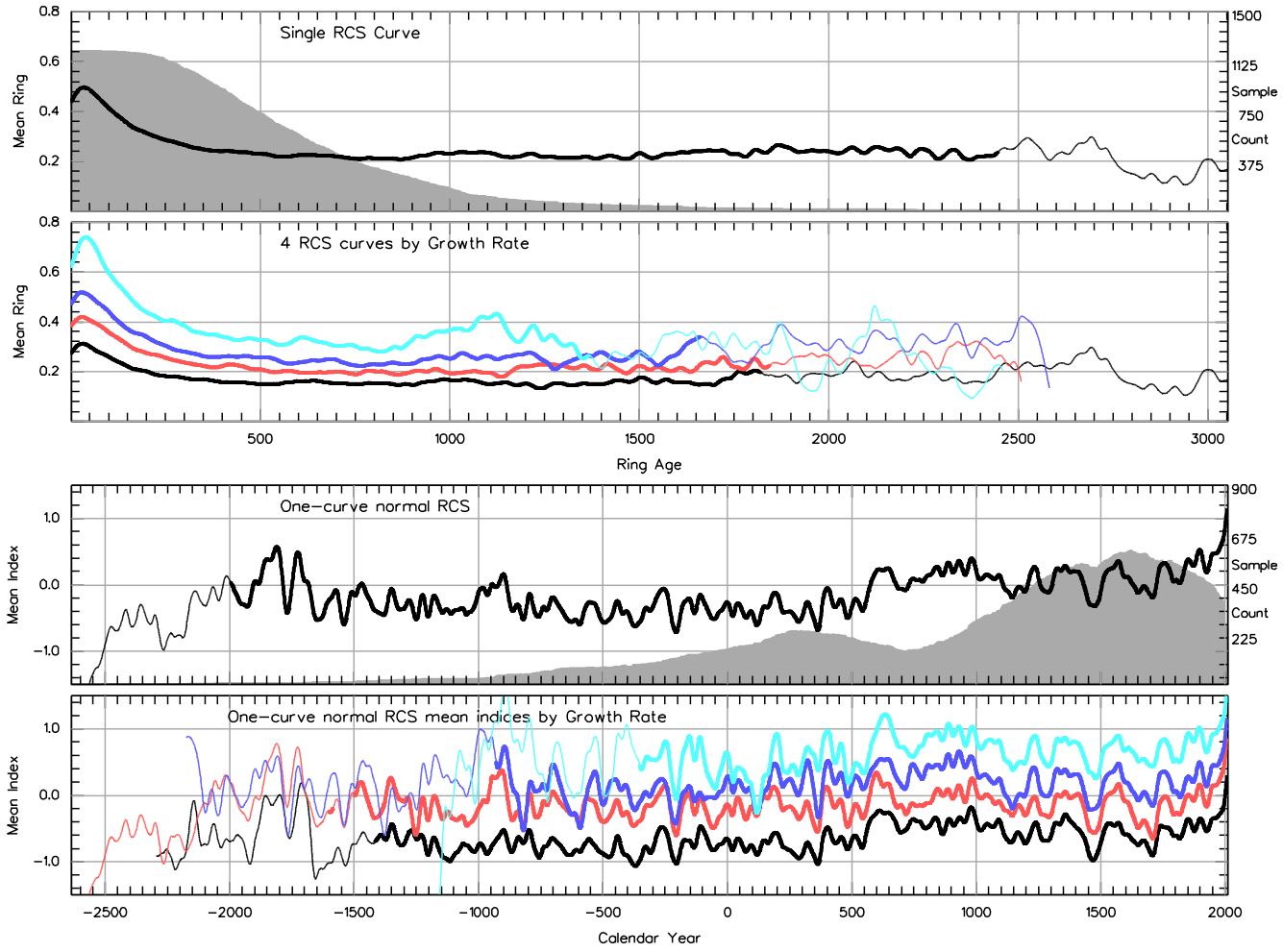

Fig. SB5. The combined data for the QLS sub-sites (DLH, GM, HYG, ZMSX, Dulan, Chin005 and Chin006) were standardised with one-curve normal SF RCS. The single RCS curve is shown in the upper panel. Signal-free measurements were averaged into four growth rate classes and the four separate growth rate curves are shown in the second panel. The single curve (simple RCS) chronology is shown in the third panel. Series of tree indices for each separate growth rate class were average by calendar year and are shown in the lowest figure. Chronologies and mean ring-width curves have been smoothed with a 50-year spline. Thin lines represent poorly replicated sections of the curves with less than 6 trees. The grey shading shows the sample (tree) replication.

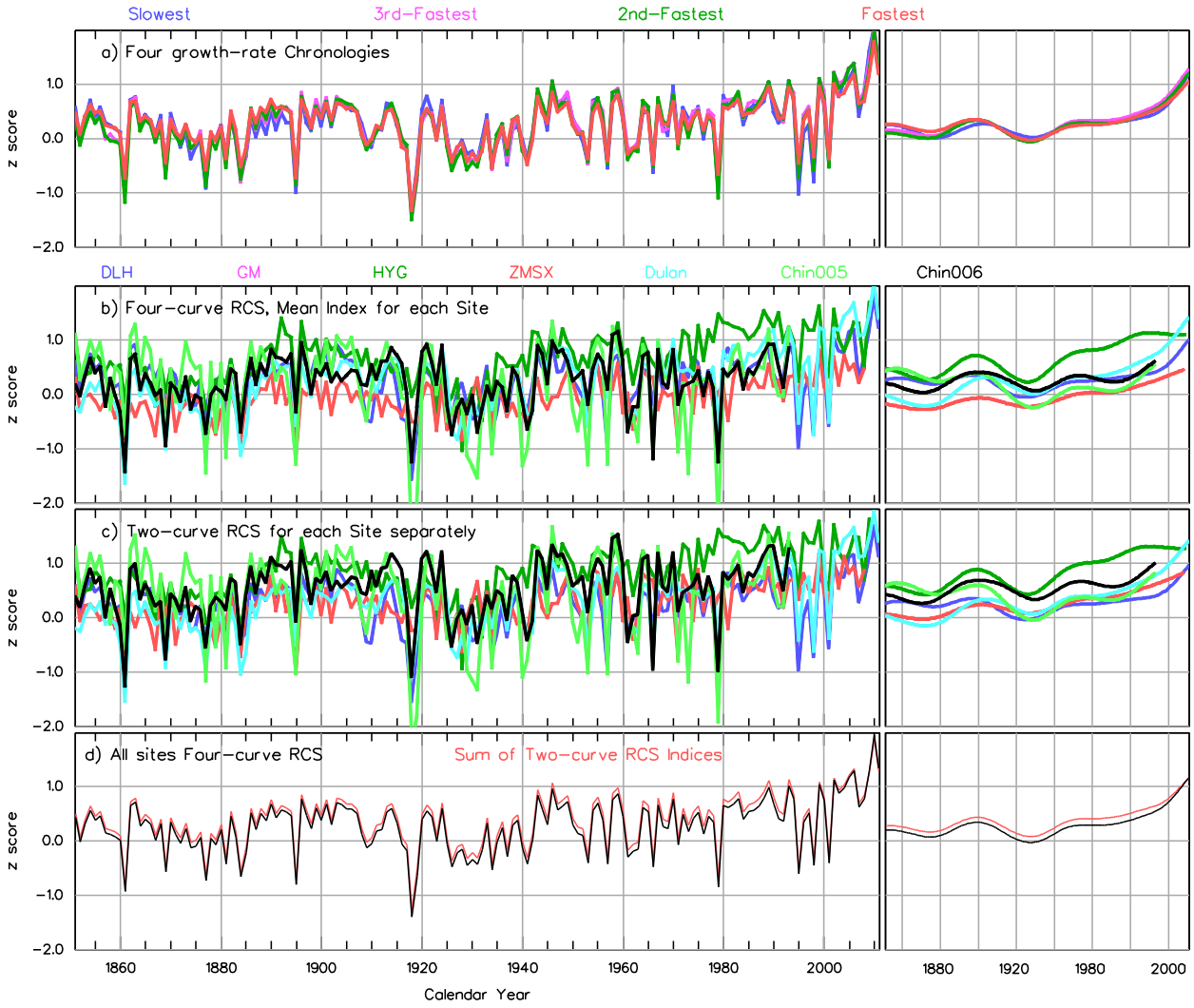

Fig. SB6. (see also Fig. 2, main paper) Recent sections of chronologies formed by averaging tree indices (i.e. standardised tree-ring width) across different subsets of trees and using different SF RCS standardisation approaches. (a) Four growth-rate chronologies (an equal number of trees are assigned to each set, grouped according to their mean growth rate) each standardised with a separate SF RCS curve. (b) Six modern site chronologies, each created by averaging the indices (obtained using the four overall growth-rate SF RCS curves) for that site. (c) Six modern site chronologies, where each site dataset was standardised using two growth-rate SF RCS curves. (d) Overall QLS chronologies formed from either the four growth-rate chronologies (black) or the six site chronologies (red). All chronologies are also smoothed with a 50-year spline (end values are more uncertain) and shown in right panels.

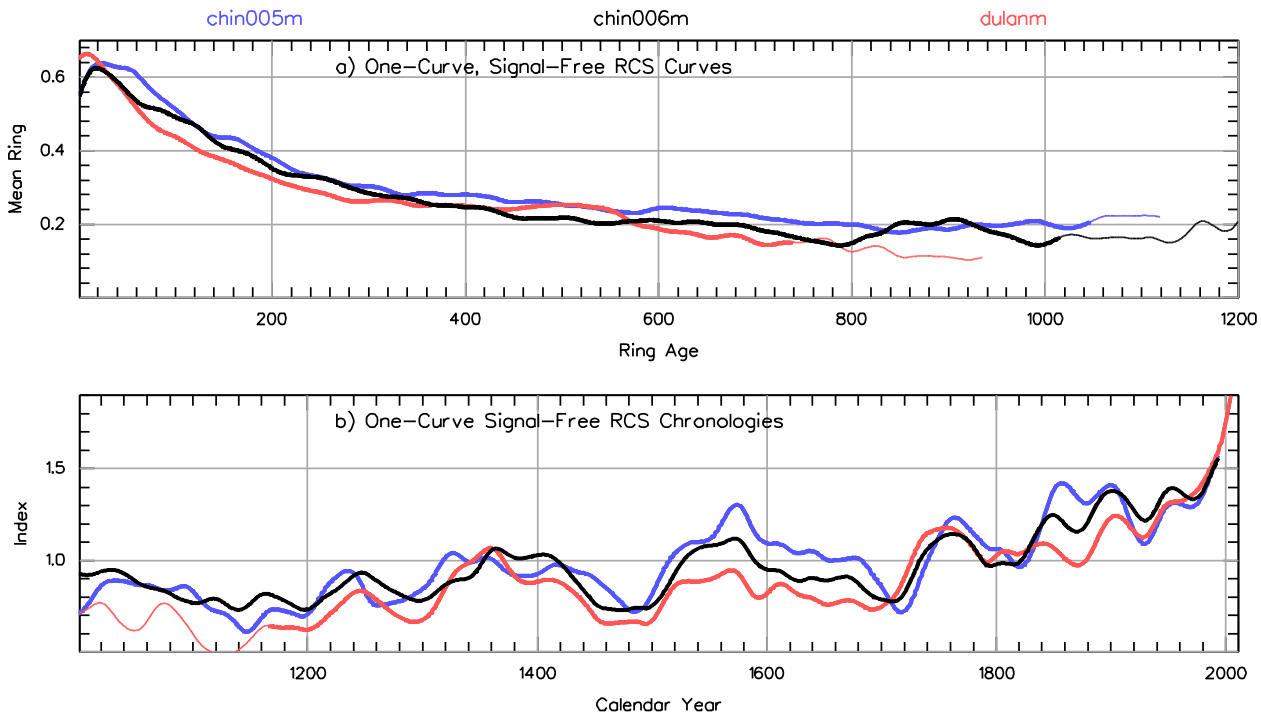

Fig. SB7. Chronologies were created independently for each of the Chin005, Chin006 and Dulan sites using one-curve, signal-free RCS. Multiple cores for any tree were averaged into mean-tree series. Comparison of mean ring-width curves (mean signal-free ring-width by ring age after 50-year spline smoothing) curves are shown in a) chin005m (blue), chin006m (black) and dulanm (red). All three data sets produce mean ring width curves with a similar shape and magnitude, although measurements from Dulan have slightly lower magnitude. The chronologies (after 50-year spline smoothing) are shown in b).

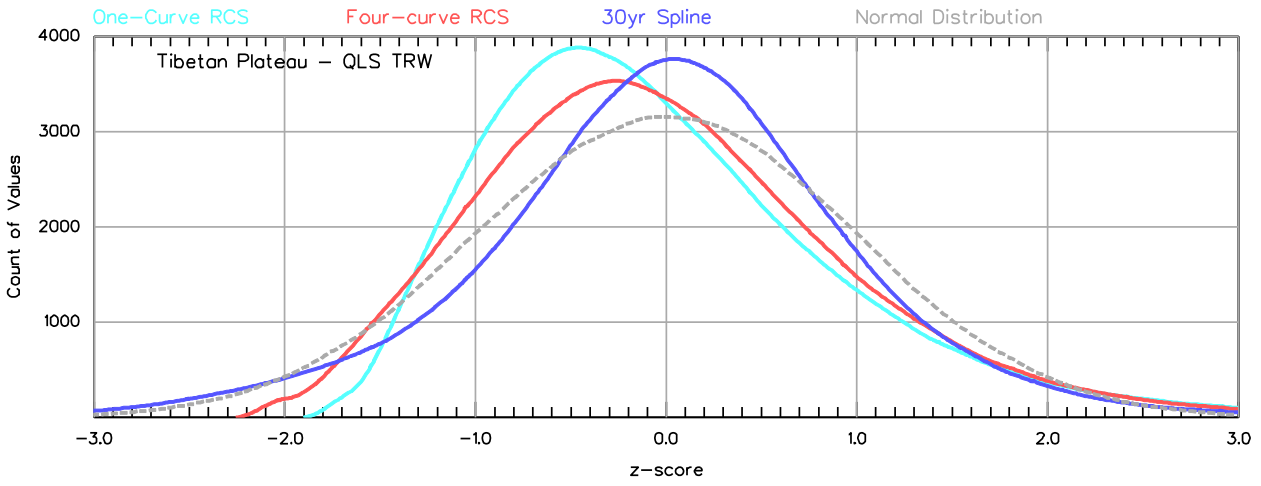

Fig. SB8. The distribution of tree-indices in various chronologies created using the QLS trees and differing methods of standardisation: one-curve SF RCS (cyan), four-curve SF RCS (red) and 30-year spline detrending (blue). Each set of tree indices has been normalised by subtracting the mean and dividing by the standard deviation. Counts of values in each 0.01 value range from -3.0 to +3.0 were smoothed with a 40-year spline. For comparison the same number of values (as for the above tree-index plots) of randomly-generated normally distributed numbers, similarly sorted and smoothed, are shown by the grey dashed line. The reconstruction we present was created using tree-indices whose values have been replaced by the values of normally distributed numbers where both series were sorted by relative magnitude (see ref. 2 for further details).

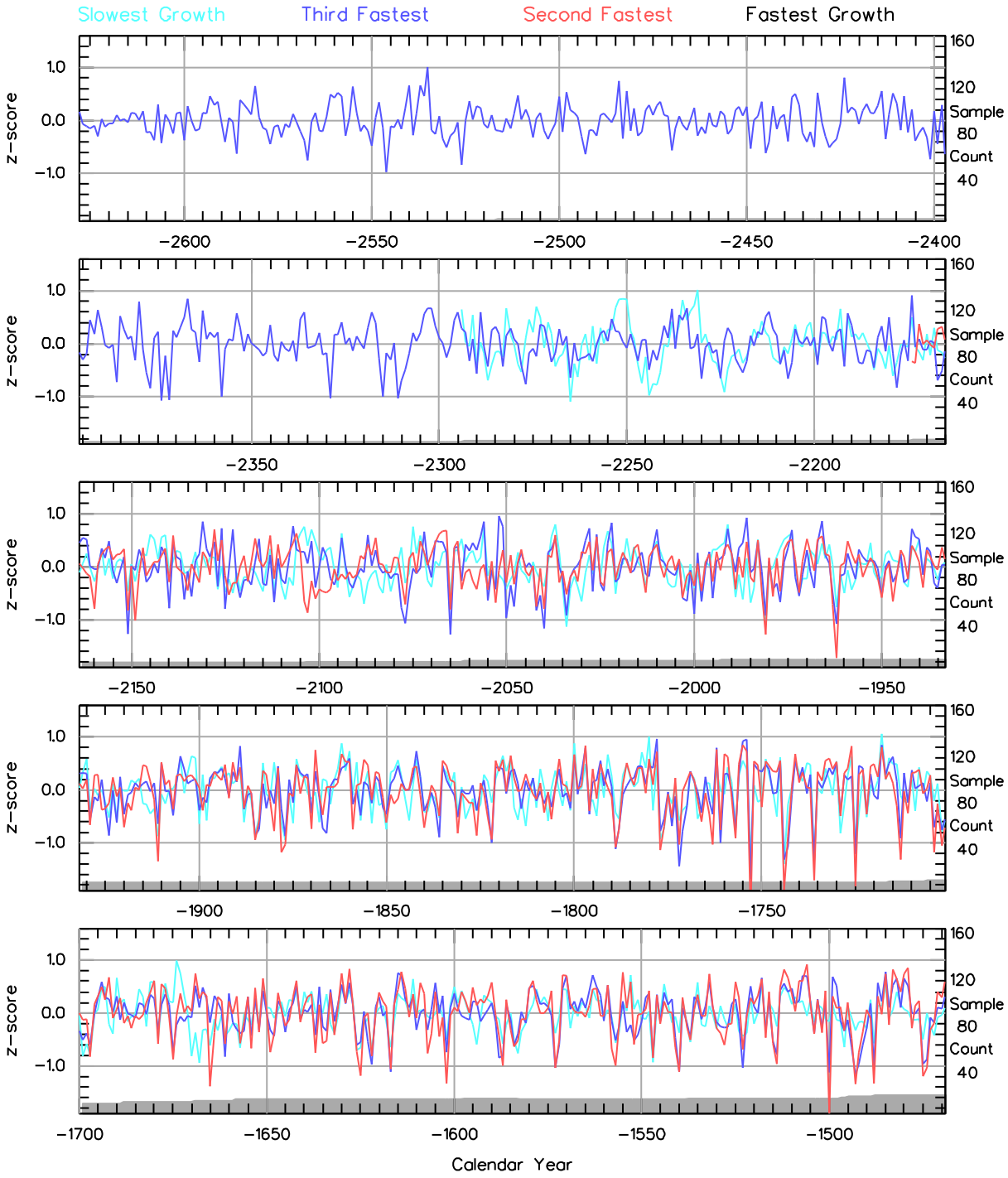

Fig. SB9. Four high-frequency growth-rate chronologies. A chronology was created using four-curve SF RCS with tree indices transformed to have a normal distribution. The four separate growth rate chronologies were high-pass filtered with a 50-year spline and plotted; slowest growth rate in cyan, 3rd fastest growth rate in blue, 2nd fastest growth rate in red, and the fastest growth rate in black. Full chronology sample counts are shown as grey shading.

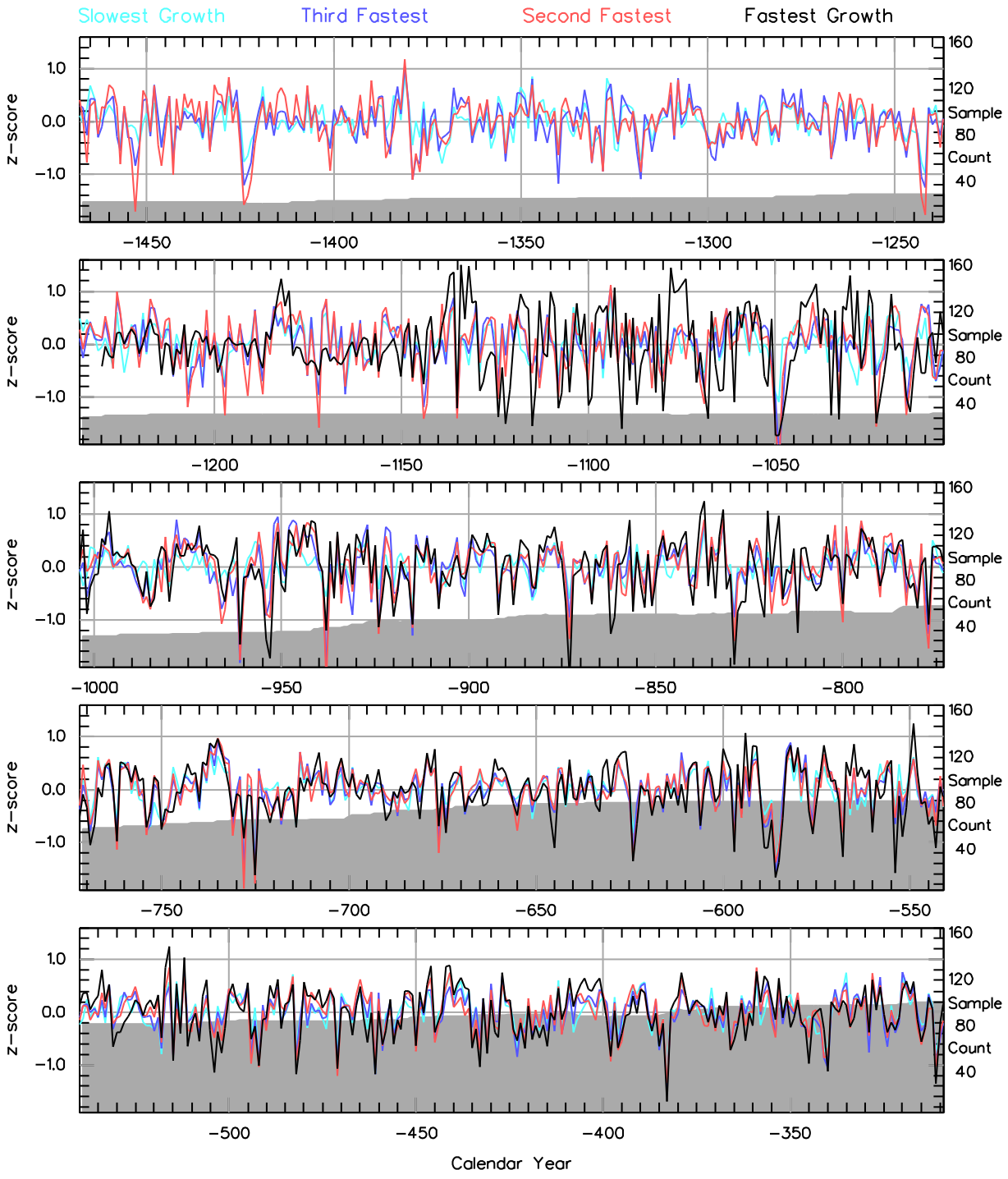

Fig. SB9. continued

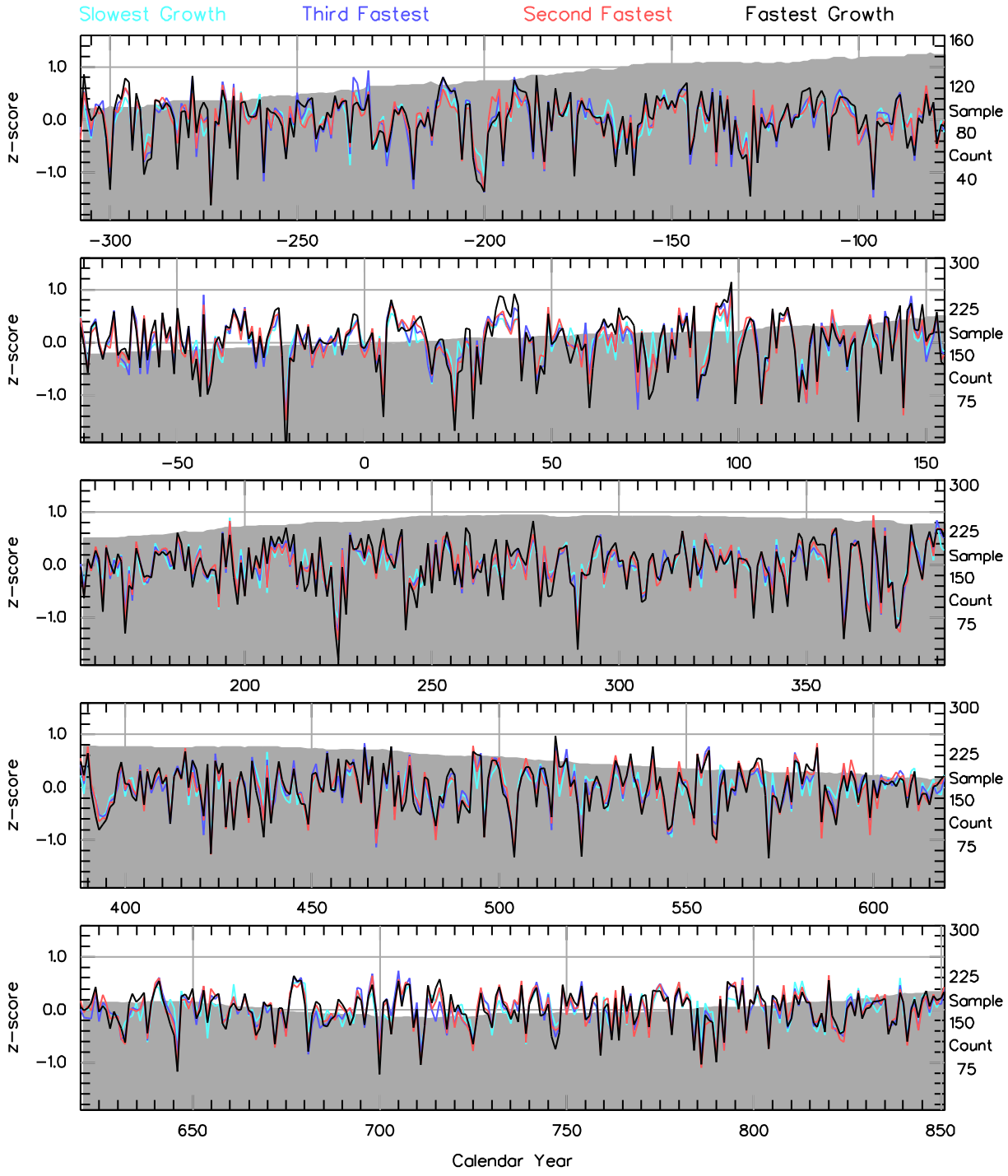

Fig. SB9. continued

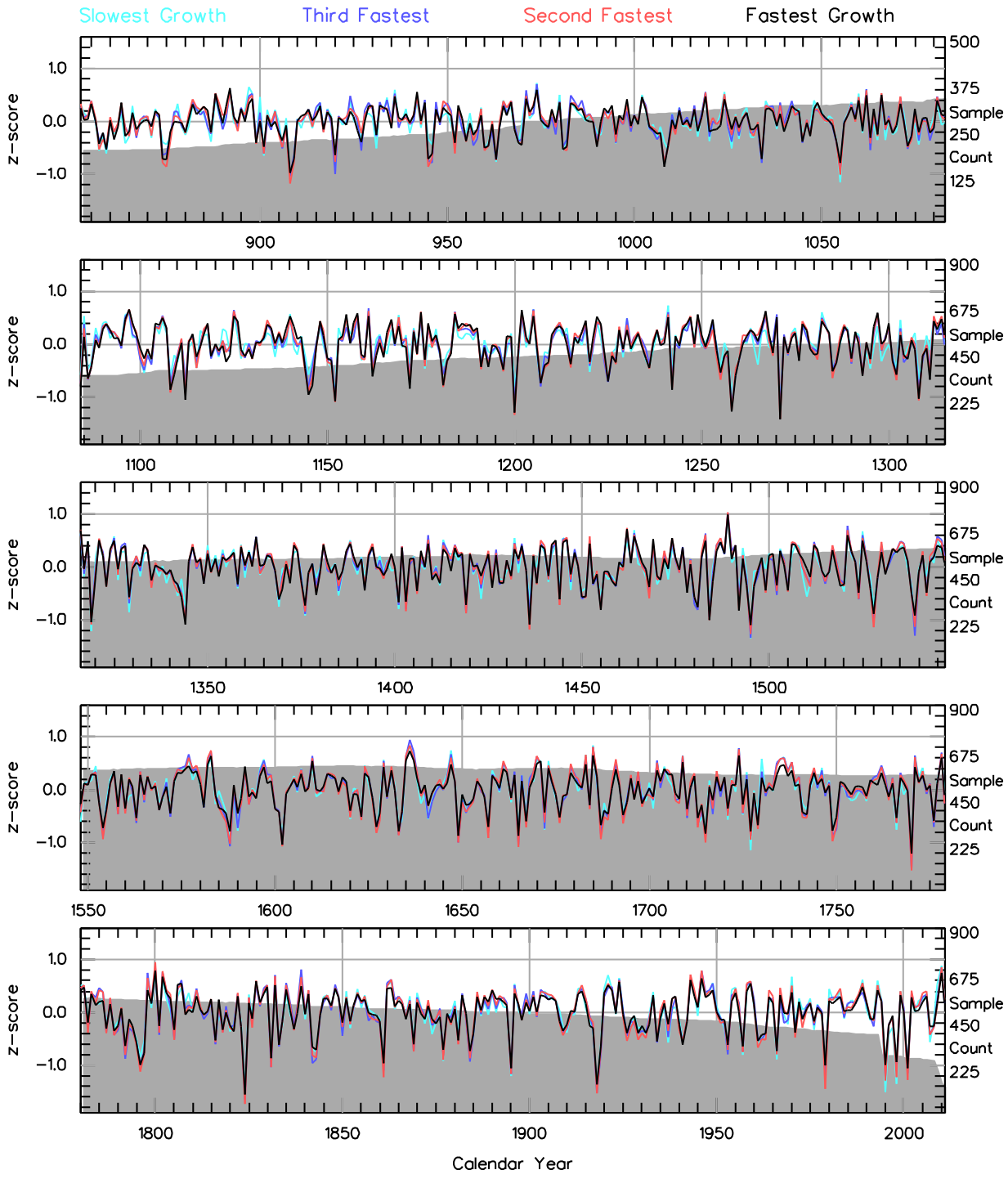

Fig. SB9. continued

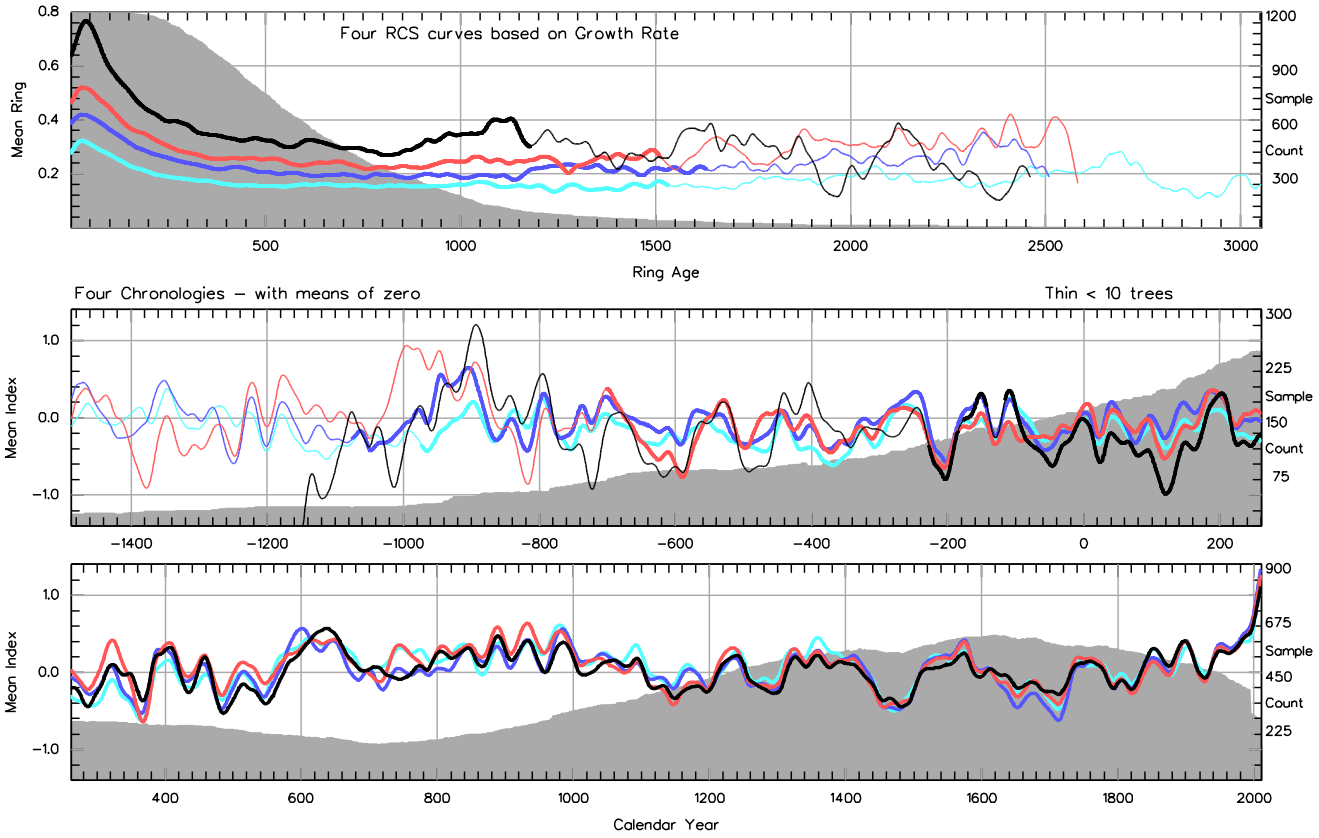

Fig. SB10. Four low-frequency growth-rate chronologies. A chronology was created using four-curve SF RCS with tree indices transformed to have a normal distribution. The mean ring width by age curves for the four RCS curves, low-pass filtered with a 50-year spline, are shown in the top panel. The four separate growth rate chronologies, low-pass filtered with a 50-year spline, are plotted by calendar year in the lower panels. The growth rates are colour coded with slowest in cyan, 3rd fastest in blue, 2nd fastest in red, and fastest in black. Full chronology sample counts are shown as grey shading.

SI Section C: Chronology presentation and comparison

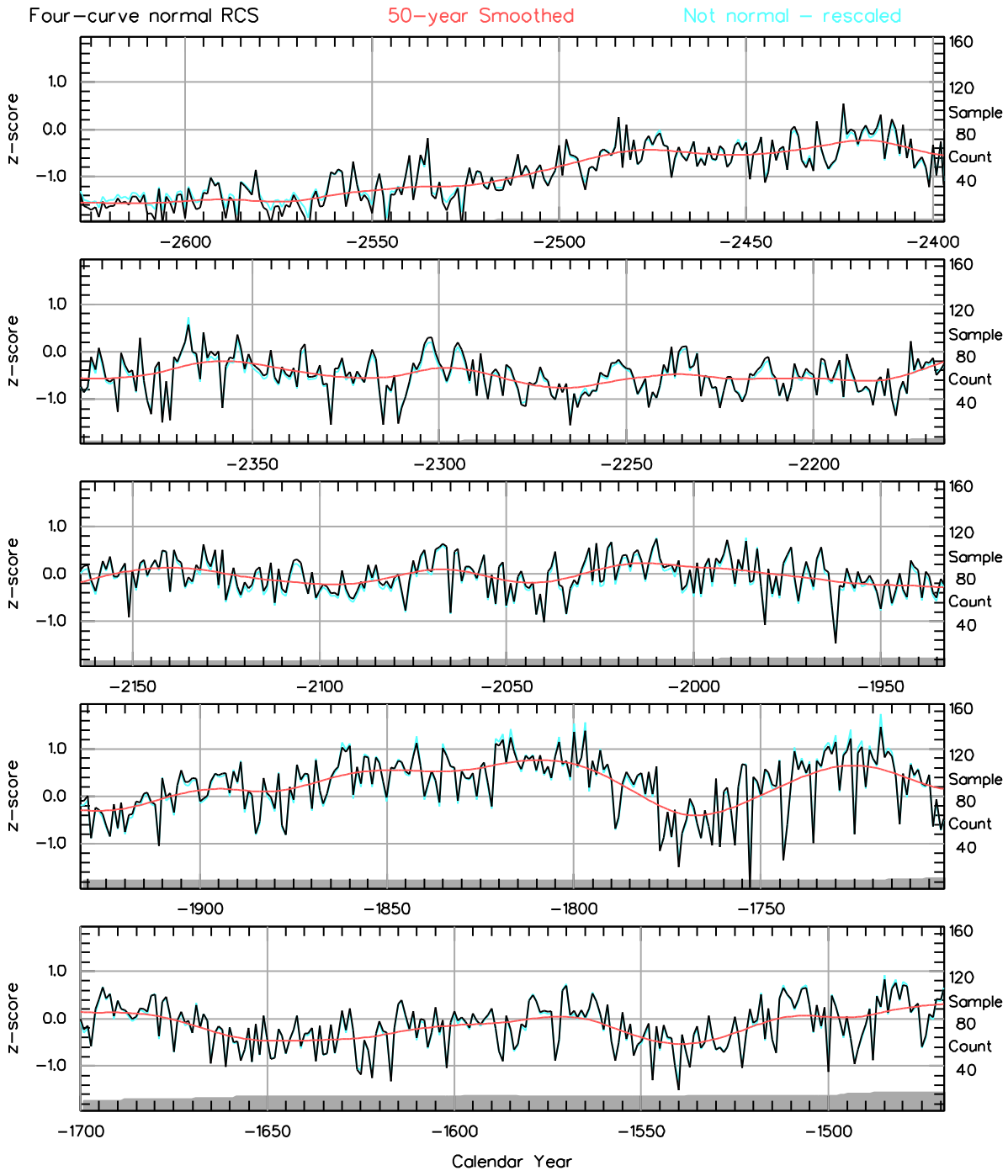

Fig. SC1. A chronology was created using four-curve SF RCS with tree indices transformed to have a normal distribution. This chronology is plotted in black with the 50-year low-pass spline values plotted in red. For comparison a chronology was created using four-curve SF RCS but without transforming the tree indices. This chronology has had its mean subtracted and has been rescaled (divided by the standard deviation of the normal chronology) for comparison and is plotted in cyan. It is important to note that before 1500 BCE the poor replication implies large chronology uncertainty (See Figures SF6 and SF7). Prior to 1850 BCE the chronology comprises only 3 trees and even cross-dating may be in doubt.

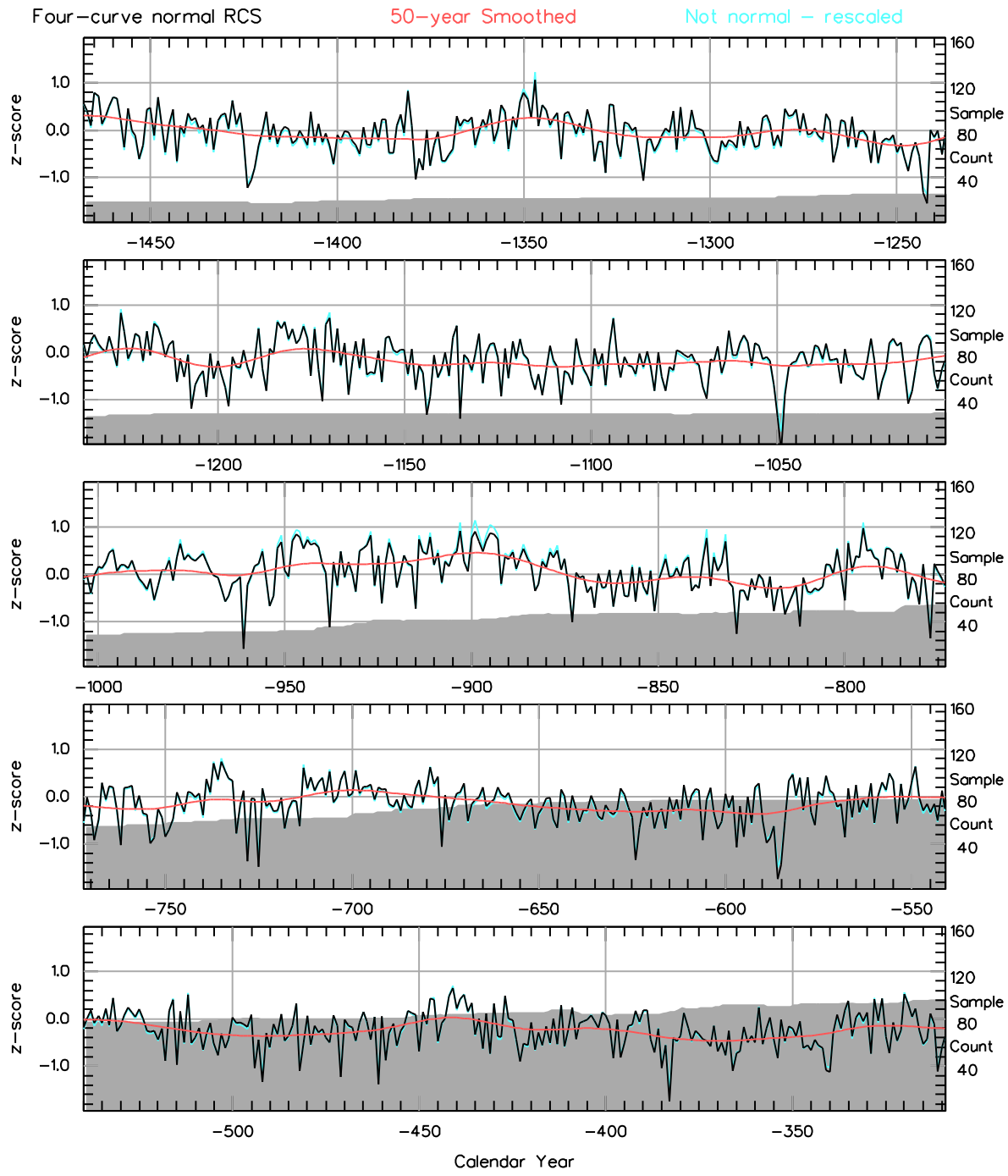

Fig. SC1. continued

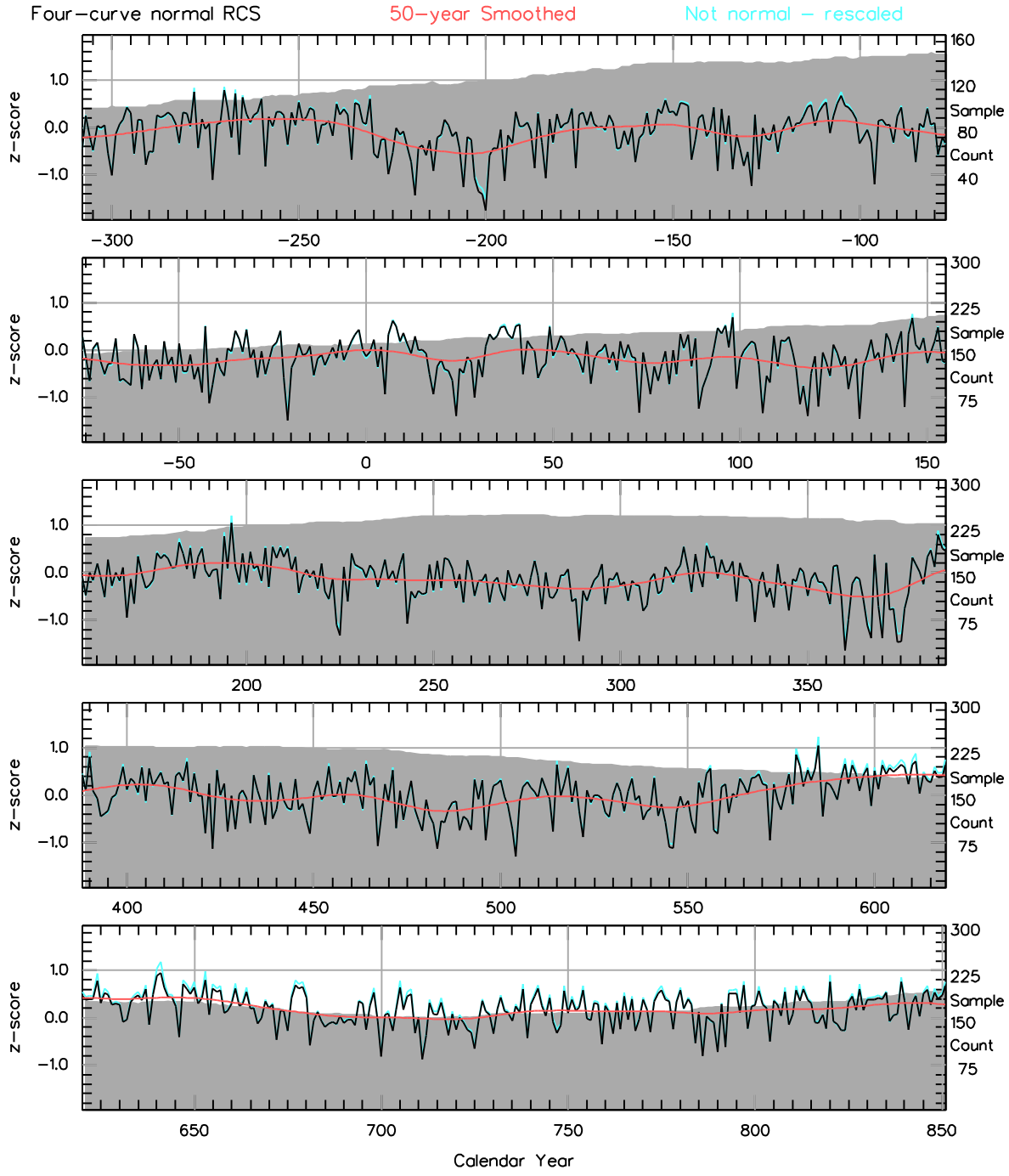

Fig. SC1. continued

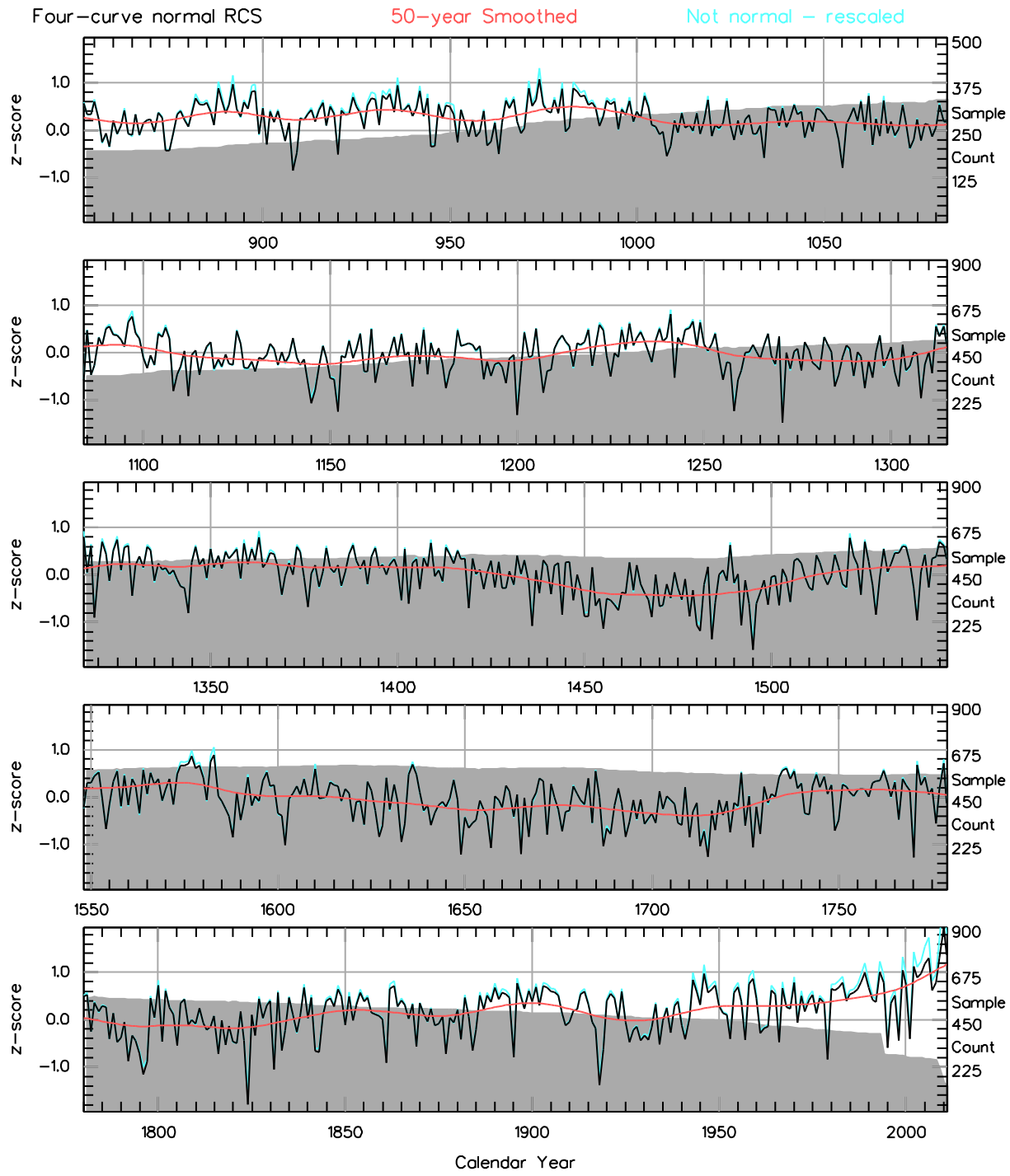

Fig. SC1. continued

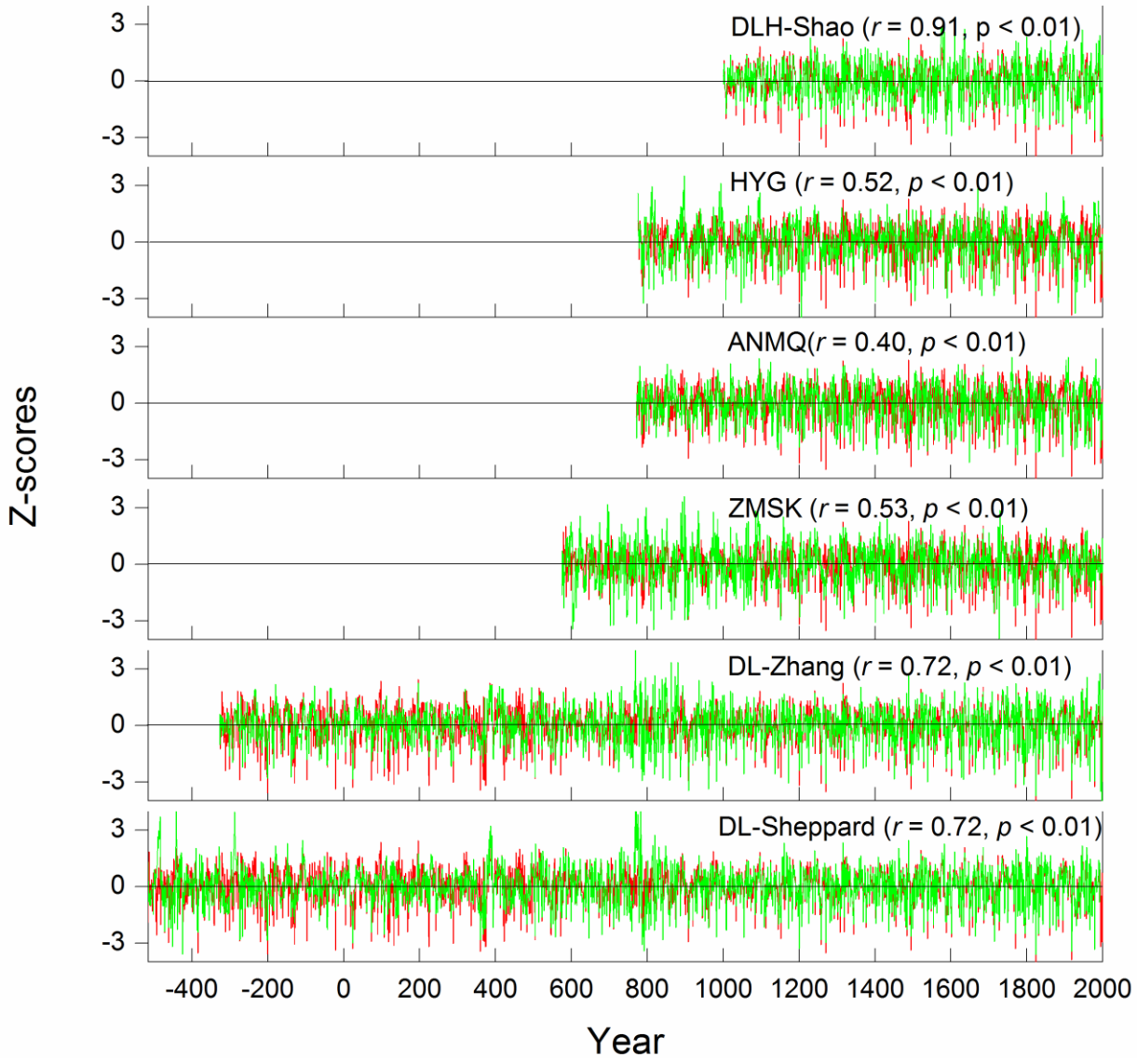

Fig. SC2. Comparison, using 100-year high-pass filtered data, of the QLS chronology (red) with other published millennia long tree-ring chronologies (green) from the north-eastern Tibetan Plateau. Only the period over which the chronologies have an EPS > 0.85 or are made up of more than 5 samples are shown. Each series has been standardized with respect to the common period 1000–1993 CE. The series are identified and other information provided in Table SC1. The comparison of our QLS ring-width chronology with the two DL chronologies suggests possible missing rings at 711 and 875 CE in DL-Zhang series (ref. 13 in the main text), and at 711 CE in the DL-Sheppard series (ref. 14 in the main text). These inferences are supported by ref. (3). In the present study, we have inserted values at these positions in the two DL chronologies using the average of the two adjacent tree-ring index values. The QLS chronology then shows highly coherent high-frequency variations with the two DL chronologies. For the 100-year high-pass filtered data, these high-frequency ring-width chronologies are significantly correlated ($p < 0.01$) with the QLS data with correlation coefficients ranging from 0.40-0.91 (see Table SC2).

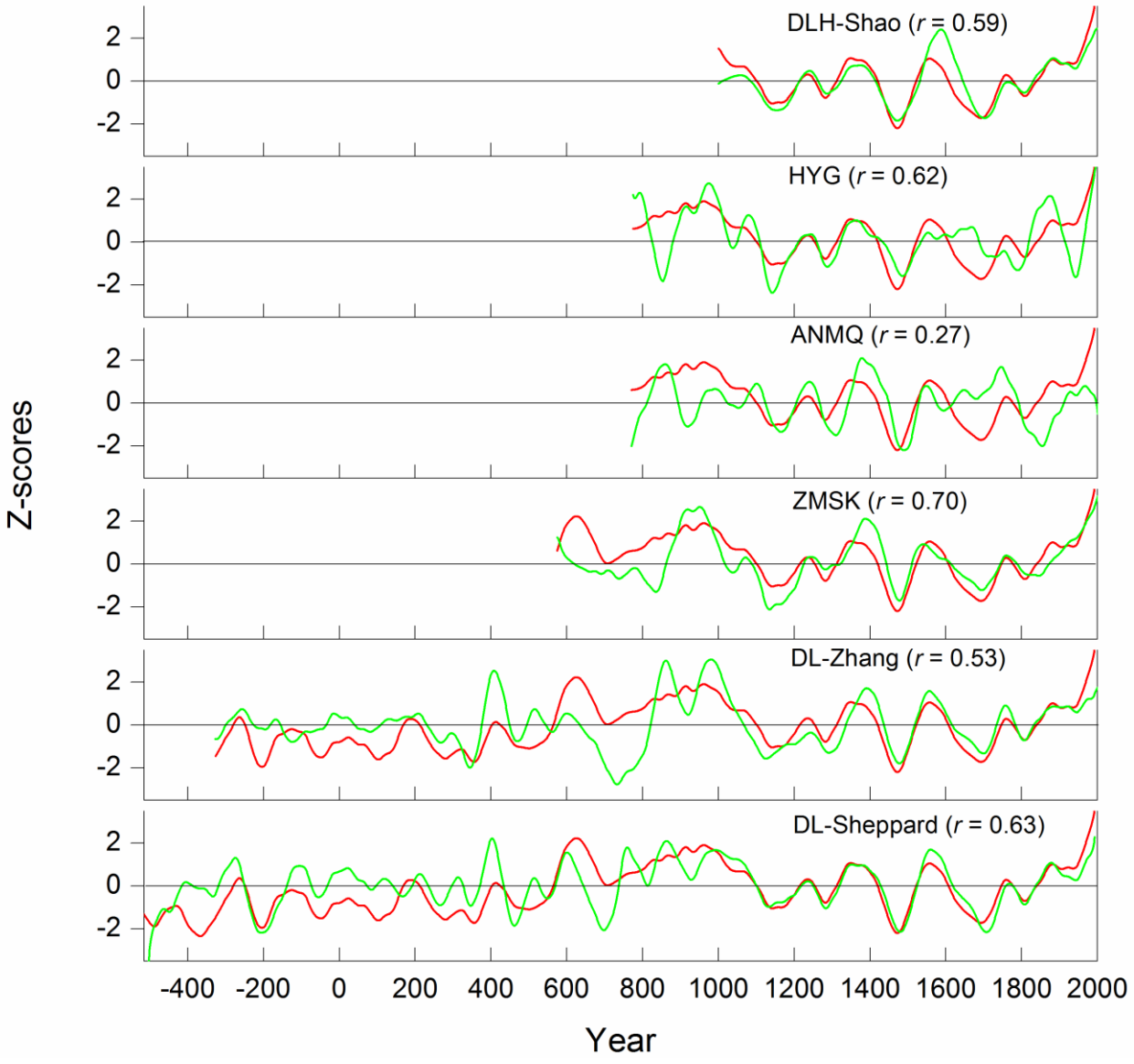

Fig. SC3. as for Fig. SC2 but showing 100-year low-pass filtered values. Note that the correlations between the QLS chronology and the other chronologies are not significant (p=0.05) after being adjusted for loss of degrees of freedom due to high mutual autocorrelation in the filtered data.

Table SC1. Meta data relating to the other millennia-long tree-ring records from the north-eastern Tibetan Plateau.

Sample area	Latitude(°N)	Longitude(°E)	Elevation (m)	Period (CE)	Data source
Haiyagou (HYG)	38.69	99.69	2950	775-2006	(4)
Animaqing (ANMQ)	34.79	100.00	3400–3700	771-2004	(5)
Zhamashike (ZMSK)	38.15	99.95	3200–3600	575-2008	ref. (17) in the main text
Delingha (DLH)	37.45	96.00	3660–3920	1000-2001	(6)
Dulan (DL1)	35.8-36.5	97.7-98.3	3100-3800	-328-2000	ref. (13) in the main text
Dulan (DL2) and Shenge	35.8-36.5	97.7-98.3	3800	-516-1993	ref. (14) in the main text

Table SC2. Correlation coefficients for comparison of 100-year high-pass-filtered millennia long ring-width chronologies on the north-eastern Tibetan Plateau.

	QLS	**DLH-Shao (*1000-2001*)**	**HYG *(775-2006)***	**ANMQ *(771-2004)***	**ZMSK *(575-2008)***	**DL-Zhang *(-328-2000)***	**DL-Sheppard *(-516-1993)***
QLS	1						
DLH-Shao	0.91	1					
HYG	0.52	0.43	1				
ANMQ	0.40	0.41	0.22	1			
ZMSK	0.53	0.42	0.55	0.30	1		
DL-Zhang	0.72	0.81	0.37	0.30	0.34	1	
DL-Sheppard	0.72	0.89	0.41	0.34	0.36	0.83	1

Note that all correlation coefficients are significant (p=0.05). Details of the abbreviations and related information for each series are provided in Table **SC1**.

SI Section D: chronology calibration

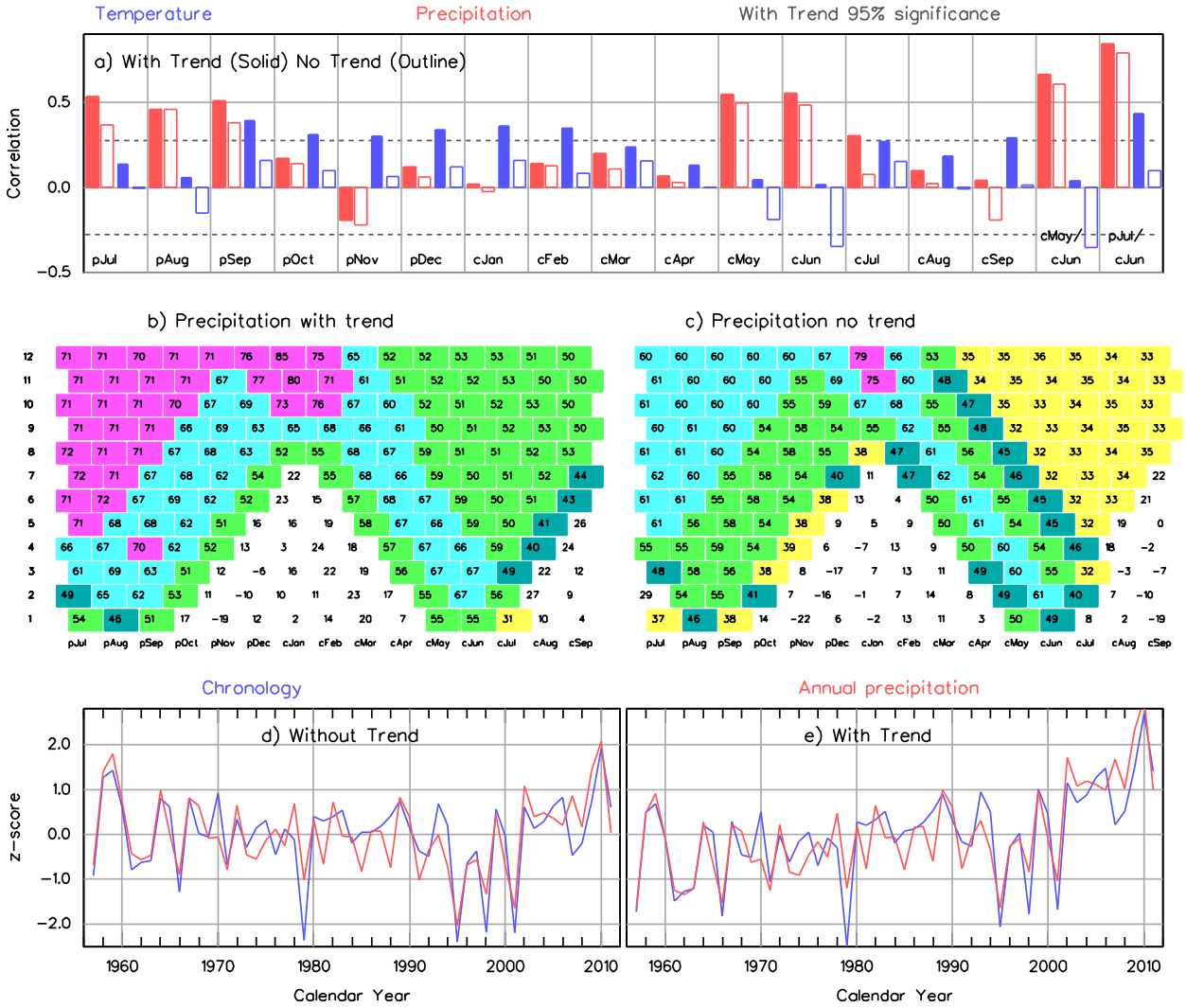

Fig. SD1. Pearson correlations between the QLS tree-ring chronology and climate. (a) Correlations between the chronology and temperature (blue) or precipitation (red), for each month from the July prior to tree growth through to the September concurrent with tree growth, and for two seasonal averages (concurrent May to June, and prior July to concurrent June). Correlations are shown for data from 1956 to 2011, with (outline bars) or without (solid bars) removal of the linear trend from each dataset. The horizontal dashed lines indicate the $p<0.05$ significance level. Significant associations are apparent between chronology and precipitation for each of the months July, August, and September of the year prior to ring formation and in May and June of the year concurrent with growth. Predominantly positive correlations (though individually not significant) are apparent for the intervening months. (b) Correlations (×100) between the QLS chronology and seasonal average precipitation for all seasons with lengths from 1 to 12 months (left-hand scale) with the centre of the seasonal average lying between the prior July and the concurrent September. Colour shading is used to highlight seasons with a correlation of at least 0.3. (c) As (b), except correlations are calculated after the chronology and precipitation have been linearly detrended. (d) Normalised time series of the linearly detrended QLS chronology (blue) and the similarly detrended annual precipitation (prior July to concurrent June, red) for the overlap period 1957–2011. (e) As (d), but showing the data without detrending.

Reconstruction Calibration – Additional description

Multiple methods of scaling the QLS tree-ring chronology to represent annual (prior July to current June) regional precipitation were compared: (i) regressing the QLS data on the precipitation data, and then scaling the QLS data by the inverse of the regression coefficient; (ii) regressing the precipitation data on the QLS data; and (iii) scaling the QLS data so that its mean and variance match those of the precipitation data. The last approach produces a scaling factor (slope coefficient, β) that is intermediate between those produced by (i) and (ii). For each of these three cases the scaling was applied in 4 ways: (a) using the original QLS and precipitation time series; (b) using linearly detrended timeseries; (c) using high-pass (< 10 years) filtered time series; and (d) using linearly detrended timeseries that were then smoothed with a low-pass (> 10 years) filter. In all cases, using the calibration data for the period 1957 to 2011.

The results for the different calibrations (shown as scatter diagrams; Fig. SD2) are all similar, with the explained variance (r^2) ranging from 61% (high-pass filtered case) to 79% (detrended, low-pass filtered case). When expressed as the deviation in mm of annual rainfall represented by one standard deviation (SD) of the chronology, the scaling coefficients (β) range from 33 to 65 mm/SD. The reconstruction shown in the main paper (Fig. 3) is based on the case with $\beta = 45$ mm/SD; detrended $r = 0.79$, i.e. case (iii)(b).

The blue shading in Figs. 3a,b in the main paper and in SD3 represents the scaled chronology uncertainty, specifically +/- 2 times the chronology standard error (i.e. the SD of all tree index values in each year divided by the square root of the number of trees in that year) scaled by the same β (i.e. 45mm SD) used to produce the reconstruction. The same scaled chronology error is used for all timescales (i.e. for unsmoothed estimates and for 10-year or 50-year smoothed values). The scaled chronology error is not sufficient to explain all of the differences between scaled chronology and precipitation data (i.e. the SD of the residuals is greater than the scaled chronology error). This implies that the total reconstruction error is composed of the chronology uncertainty and an additional "precipitation representation uncertainty": even if the chronology were perfect, it would not represent annual-mean precipitation exactly. The total reconstruction error is then formed by combining the scaled chronology error and the precipitation representation uncertainty in quadrature. The latter is estimated by assuming that, over the calibration period, the total reconstruction error is equal to the SD of the residuals (i.e. precipitation minus estimated values). The pink shading (Figs. 3a,b in the main paper and in SD3) is +/- 2 times the total reconstruction error, obtained by combining in quadrature the scaled chronology uncertainty (which changes over time as the number of constituent index series in the chronology varies) with the precipitation representation uncertainty (which is kept constant over time).

The precipitation representation uncertainty (and hence the total reconstruction error) is computed separately for the unfiltered data and for the 10-year smoothed data. It is smaller for the 10-year smoothed data because the unfiltered residuals have near zero lag-one autocorrelation and so some cancellation of uncorrelated errors would be expected when they are averaged (i.e. smoothed) in time. Note that the error is reduced by less than $\sqrt{10}$, so the error estimates are not as small as if we had assumed the errors were simply white (uncorrelated) noise. The 50-year smoothed plots use the same errors as estimated for the 10-year smoothed results. In reality there might be some further reduction in the random component of the error due to the additional time averaging, but there would probably also be an increase in chronology error at timescales longer than 50 years.

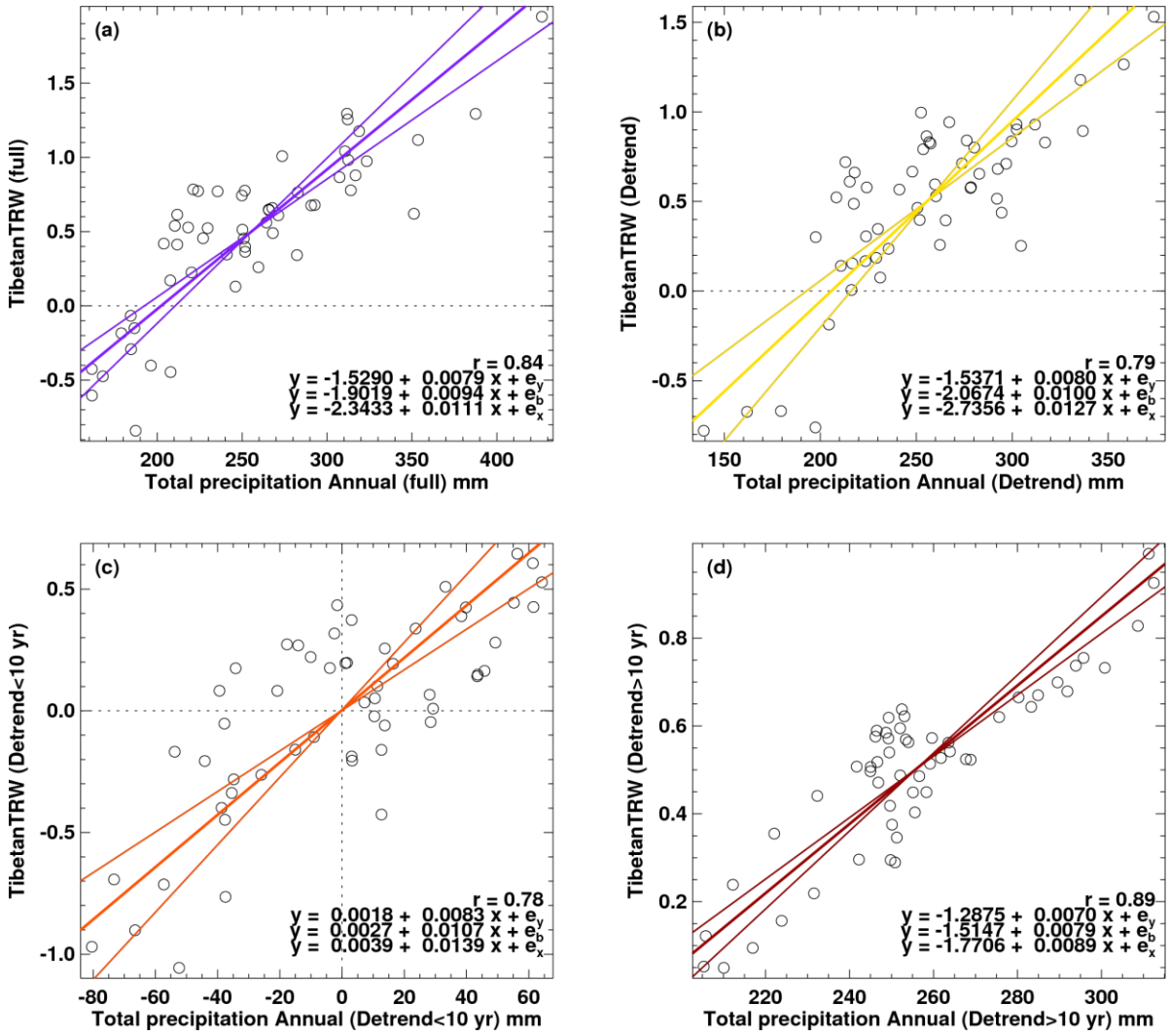

Fig. SD2. Scatter plots for various calibrations of the QLS chronology: all showing TRW (y-axis) vs. annual (previous July to current June) precipitation (x-axis): using original data (top left); both datasets linearly detrended over 1957-2011 (top right); both datasets high-pass (<10 year) filtered (bottom left); and both datasets detrended and then smoothed with low-pass (>10 year) filter (bottom right). In each case, there are three calibration lines: y-on-x, x-on-y, and the intermediate that scales the chronology so that its variance is the same as the precipitation variance. The reconstruction is based on the intermediate line of the top-right panel – i.e. variance matching using data that have been linearly detrended but not filtered (see Methods in the main paper).

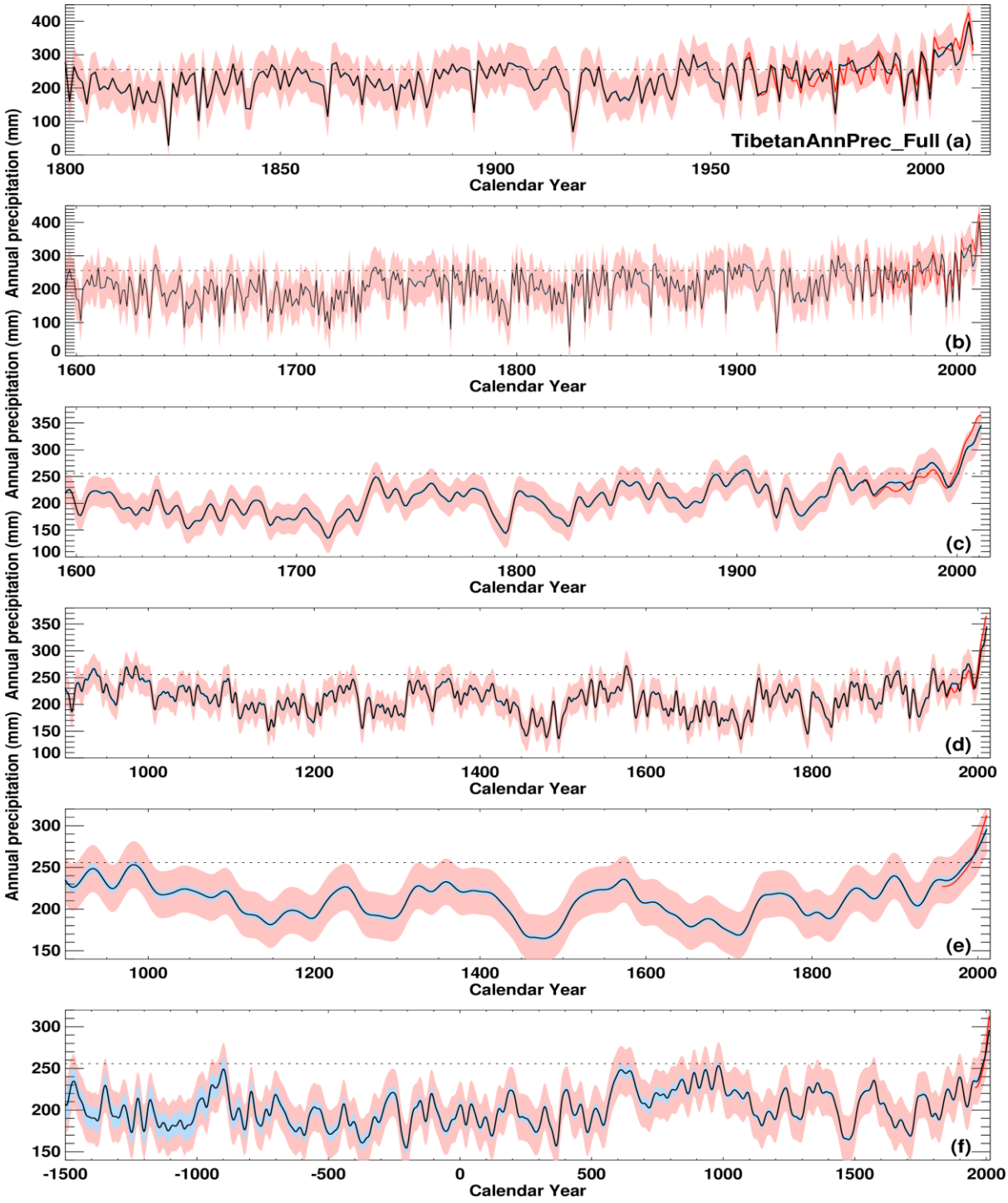

Fig. SD3. The reconstruction estimates and observed regional precipitation shown for various time periods and degrees of smoothing (see Fig. 3 in the main paper): (a) 1800-2011, no smoothing, (b) 1595-2011, no smoothing, (c) 1595-2011, 10-year smoothing, (d) 900-2011, 10-year smoothing, (e) 900-2011, 50-year smoothing, (f) -1500-2011, 50-year smoothing. Note that the values near to the ends of the smoothed series are more uncertain than shown because of filter end effects. Black lines are the reconstruction central value, red lines are instrumental precipitation. The pale blue shading is +/-2 times the chronology standard error (=standard deviation of all tree index values in a particular year divided by square root of the number of trees in that year), scaled by the same calibration coefficient as the reconstruction. The blue shading is the same in all panels i.e. there is no change between unsmoothed, 10-year smoothed or 50-year smoothed data.

Cross-validation of the annual precipitation reconstruction

The reconstruction of precipitation presented in the main part of this paper is obtained by scaling the final QLS chronology so that the chronology (linearly detrended over the 1957–2011 period) has the same mean and variance (calculated over the 1957–2011 period) as the similarly detrended regional annual precipitation series (also over the 1957–2011 period). The scaling factor was applied to the full chronology (i.e. without any detrending over the 1957–2011 period). This procedure is unlikely to suffer from any "over-fitting" issues because it involves neither the selection of a particular statistical model from a choice of possible models nor the fitting of multiple parameters within the model (as would be the case with a multiple regression model). The calibration performance is, therefore, likely to be a fair representation of the reliability of the reconstruction (taking into account, as we have, the deterioration in performance expected when the sample replication is lower early in the chronology, and the other caveats stated in the paper).

Nevertheless, we have also undertaken a cross-validation exercise, which demonstrates that the relationship between the QLS chronology and the regional annual precipitation is relatively stable over the 55 years for which we have overlapping data (1957–2011). We use a "leave-one-out" cross-validation, where each value in the available data is, in turn, treated as the validation data and the remaining values as the calibration data (or training set). This is preferable to splitting the available data into two sets, one for calibration and the other for validation, when the sample size is already quite small (55 annual values). Leave-one-out cross validation can yield inflated estimates of reliability in the presence of trends or autocorrelation, because each omitted value is not independent of the neighbouring values which form part of the calibration set. This effect is likely to be small in our case, because we are using detrended data for the calibration. Nevertheless, we repeated the cross-validation exercise and removed an additional N values (i.e. a gap size of N) either side of each validation value, and these additional data values were not used for either calibration or validation. This reduces any dependency between the validation values and their neighbouring values, because the nearest neighbour will be N+1 years away from the validation value.

The results of this exercise are shown in Figure SD4 for the case where $N = 0$ (i.e. no gaps between calibration and validation values) and in Table SD1 for cases with a range of gap sizes. Although the calibration is always made using detrended data, the scaling factor is applied to the non-detrended QLS chronology to obtain the precipitation reconstruction. The cross-validation is, therefore, applied to both detrended and non-detrended data (but calibration is always made using detrended data). Results for both cases are included in Figure SD4 and Table SD1. The cross-validation is assessed using two measures of similarity: the Pearson correlation coefficient and the Reduction of Error (RE). The latter is a more powerful test statistic, penalising errors in the amplitude (from the mean level of the calibration period) of predicted values:

$$RE = 1 - \sum(y_i - \hat{y})^2 / \sum(y_i - y_{cl})^2$$

where y_i is the observation in year i, $\hat{y}$ is the predicted value for validation, and y_{cl} is the mean of the observations during the calibration period (i.e. using all data except for the omitted observation from year i).

The top panel of Figure SD4 demonstrates the stability of the calibration scaling factor as each value is left out in turn. The middle panel demonstrates the close correspondence between the TRW chronology and regional annual precipitation in this area, even when taking a cross-validation approach. It demonstrates that this association is not the result of any over-fitting (which is anyway

not likely to be a problem with simple univariate linear regression). The poor fit during the 1980s is not a result of cross-validation; instead it is a period where the TRW and precipitation data do not follow each other very closely. Despite using detrended data, there is still some autocorrelation in both datasets, principally arising from a downward 1955–1995 downward slope followed by an upward slope. For this reason, the cross-validation results in Table SD1 for gaps up to $N = 10$ years provide a useful check. The cross-validated data maintain high correlations and RE values throughout. Finally, the bottom panel of Figure SD4 and right-hand half of Table SD1 show the results when applied to non-detrended data. The overall trend in predicted precipitation matches quite closely with the trend in the precipitation observations, despite the calibration being based only on detrended data. The cross-calibration statistics again remain strong.

Table SD1. Results of the cross-validation exercise, correlation coefficient (*r*) and Reduction of Error (*RE*). *RE* compares the predicted and observed values, relative to the mean of the calibration data; in cross-validation, the calibration data mean changes for each validated value because the calibration data changes.

	Detrended validation		Non-detrended validation	
Gap size, *N*	*r*	*RE*	*r*	*RE*
0	0.78	0.57	0.83	0.69
1	0.78	0.58	0.83	0.70
3	0.78	0.58	0.83	0.71
5	0.78	0.59	0.83	0.73
10	0.77	0.60	0.83	0.76

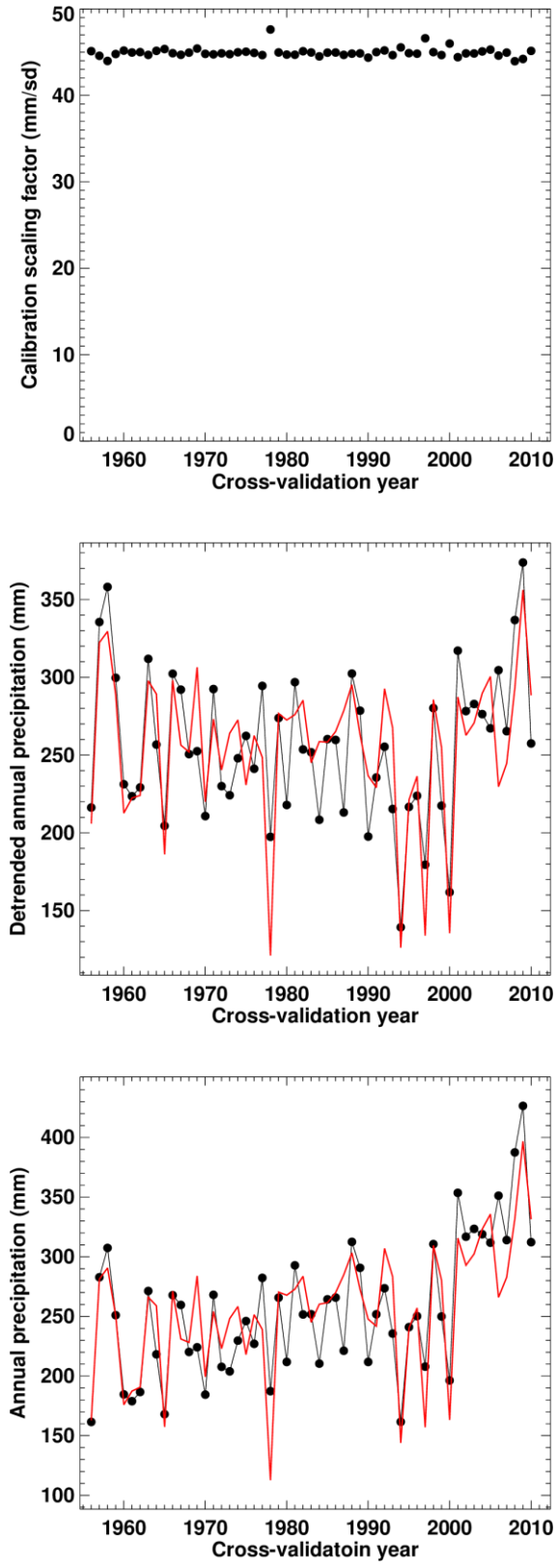

Figure SD4. Results of the cross-validation exercise, for the case where there is no gap between the training data and the validation values: (top) the scaling factor obtained from the training data with the validation year omitted; (middle) the detrended precipitation observations (black dots connected by black lines) and the values from the cross-validation exercise predicted using the similarly detrended QLS chronology (red lines); and (bottom) same as the middle panel, but using precipitation and chronology data without detrending (though the scaling factors were still obtained using detrended data, omitting the validation year).

Section E: interpretation of the variability in QLS inferred precipitation

Analysis of QLS, Dongge Cave oxygen isoptopes and Total Solar Irradiance

In the main paper (see Fig. 4) we refer to the use of the Dongge Cave oxygen isotope record (ref. 27 in the main text) as a proxy for changing monsoon intensity. Analysis of the longer oxygen isotope record from the Dongge Cave site has suggested a link between Asian monsoon variability and changes in cosmogenic radionuclides (^{10}Be in polar ice cores and ^{14}C in absolutely dated tree rings). These are a proxy for received solar energy, associated with both orbital changes and variation in the total solar irradiance (TSI) (7, 8; 27 and 34 in the main text). The measured Dongge Cave δ^{18}O data become increasingly less negative over much of the Holocene which could be interpreted as a consistent weakening of the Asian monsoon with corresponding reduction in total summer rainfall, apparent for the period 7000 to 1500 years BP. The more recent Dongge Cave data suggest an overall trend towards monsoon intensification after circa 500 CE. The QLS data do not show these trends.

However, ref. (28) in the main text have demonstrated an association between the Dongge Cave and TSI series over more than 9000 years that is highly unlikely to be the result of chance: both records have only multi-decadal resolution and, after each is normalised and filtered to remove variations on timescales above 2000 years, they correlate at ~0.3, with low solar activity corresponding with inferred less-intense Asian monsoon (i.e. higher δ^{18}O). This apparent association has a random probability of less than one in a million. However, it still represents only 10% common variability over the full overlap between the two detrended series. The association between these records appears stronger during the early millennia (i.e. in the 9th to the beginning of the 5th millennia BP), but also in the 3rd millennium BP (see ref. 28 in the main text, Fig. 4a). Concentrations of variance at about 210 years (referred to as the de Vries cycle) and near 1000 years (the Eddy cycle) are highlighted in the analysis of ref. (28) in the main text.

The Multi-Taper Method (MTM) of spectral analysis (9) and wavelet analysis (10, 11) were used to evaluate the TSI and QLS records in the frequency domain. Figures SE1 and SE2 show that the spectra are clearly dominated by significant (0.05 level) spectral power in the low-frequency domain of 60-220 year band/90-320 year band for the TSI/QLS series over the common period -2637 to 1987 CE respectively. The Wavelet spectrum for the TSI (Fig. SE2b) shows significant variance in the 260-360 and circa 510-year bands during the last 4000 years and some, discontinuous 30-60 year power. Besides the concentration in variance at 60-220 years, the QLS series (Fig. SE2c) also has additional power at about 1000 years (manifest between about 1500 BCE and 800 CE) and at 510 years (2000 BCE to 500 CE). However, the coherency analysis (Fig. SE2e) shows that that the only significant co-variation between the two series that is in phase, is on a temporal scale of around 200 years, and even then, only for the last 800 years. Comparing the 5-yr resolved TSI and QLS series, the Pearson correlation is 0.63 for this period. Fig. SE3 shows the series compared after band-pass filtering (11) to isolate the circa 200-year timescale variability. While the correspondence in phase and in the modulation of quasi-periodic variability is suggestive of a link at this timescale, the clear lack of correspondence prior to 1000 argues that the recent correspondence may be by chance.

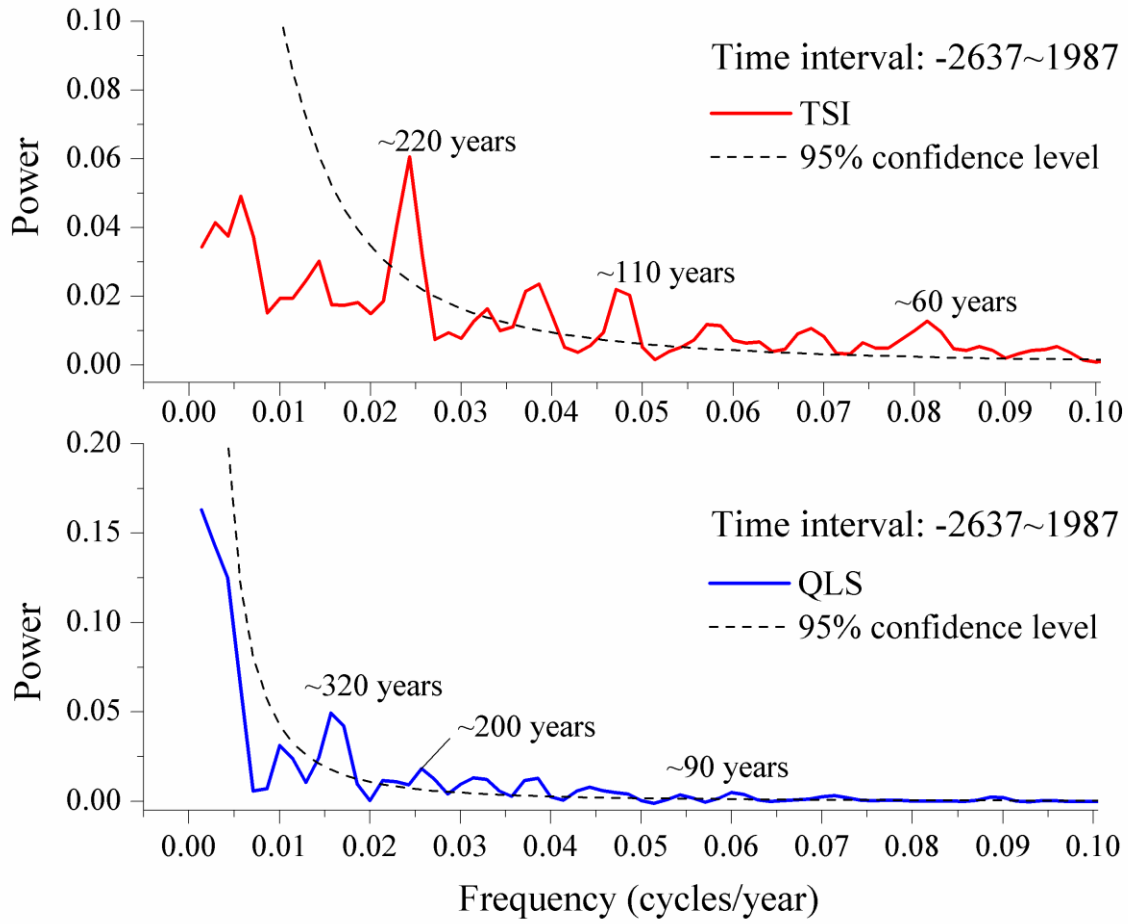

Fig. SE1. The multi-taper power spectra of the QLS series and the inferred total solar irradiance (TSI) from ref. (12) for the past four thousand years. The time resolution of QLS series has been reduced to 5-year time resolution in order to fit with TSI data. Then both records have been standardized (by subtraction of the mean value and division by the standard deviation) over the common period -2637-1987 CE.

.

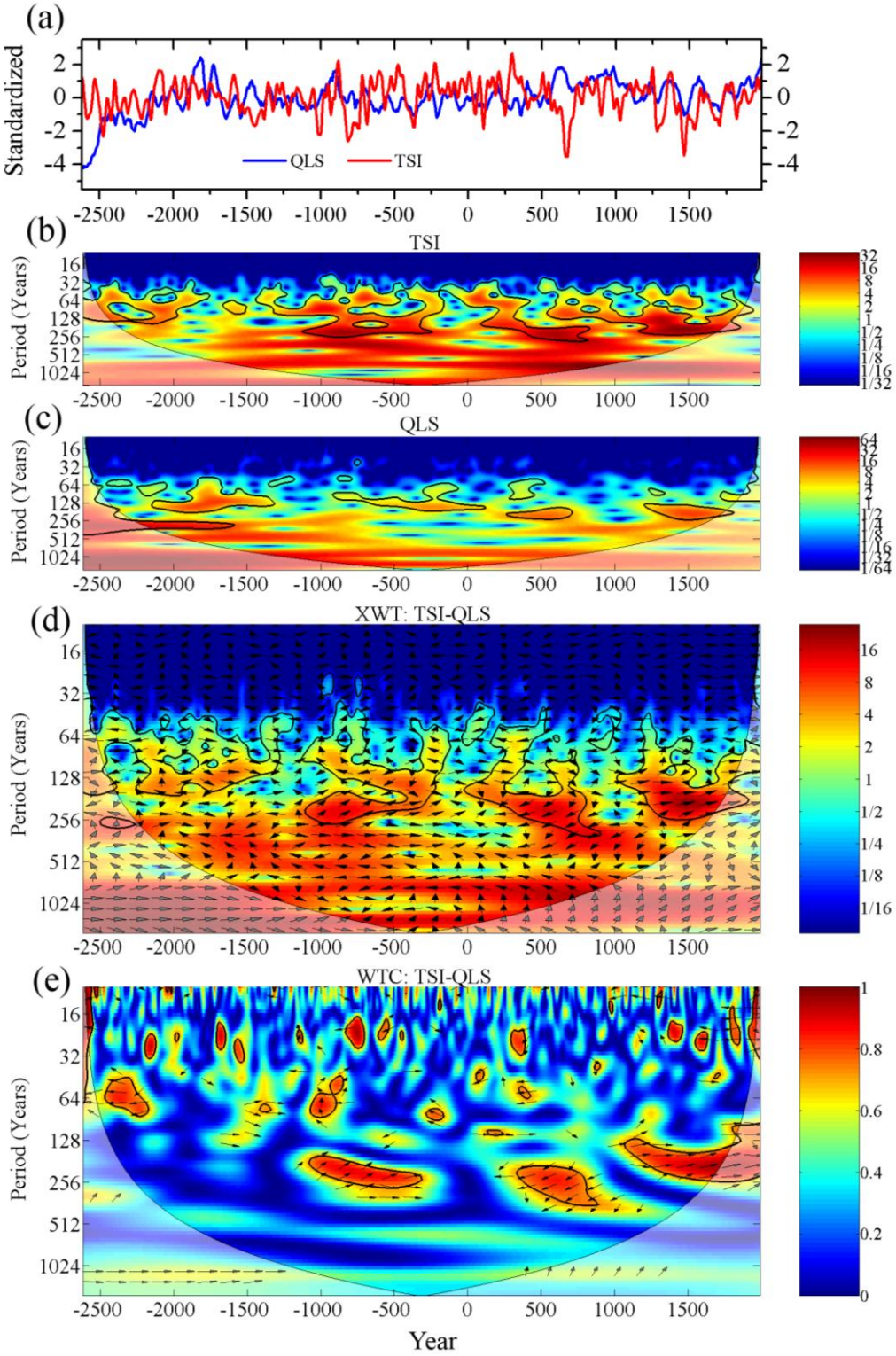

Fig. SE2. Comparison of inferred solar activity (Total Solar Irradiance, TSI) with the QLS series over the past 4650 years. Both records have been standardized (by subtraction of the mean value and division by the standard deviation) over the common period. (a) Time series of solar activity (TSI from ref. 12, red line) and QLS (blue line). (b) Wavelet power spectrum of solar activity. (c) Wavelet power spectrum of QLS series. (d) Cross wavelet transform of the two series. (e) Wavelet coherence of TSI and QLS series. Arrows pointing to the right (left) indicate that the two records are in phase (anti-phase). Black boundaries mark 95% confidence level. The right legend indicates power. The cone of influence, where edge effects might distort the picture, is distinguished by the lighter colour shading.

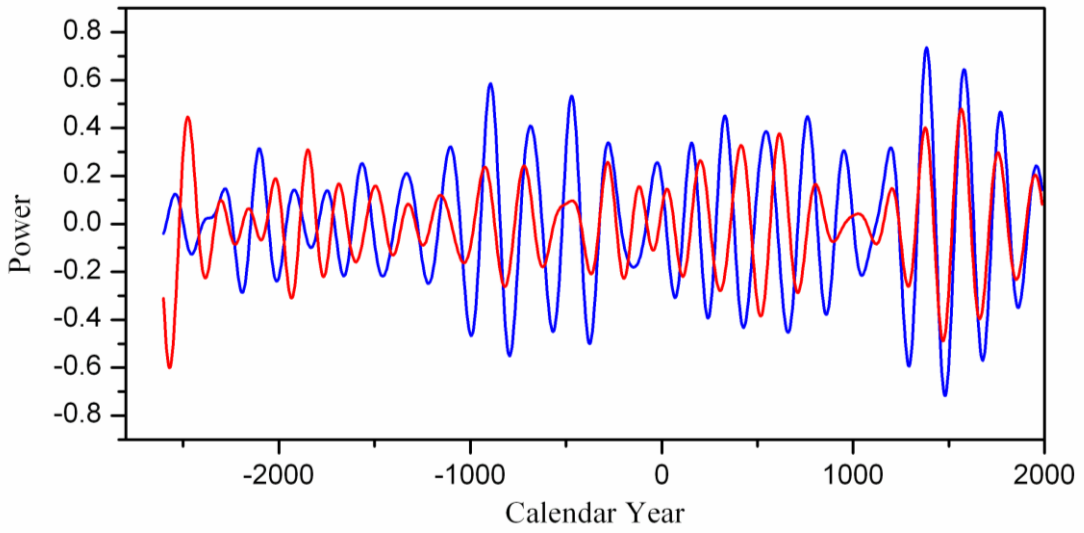

Fig. SE3. Variability of the reconstructed TSI (red) and QLS (blue) records filtered with a wavelet bandpass filter in the band widths of 170-230 yr.

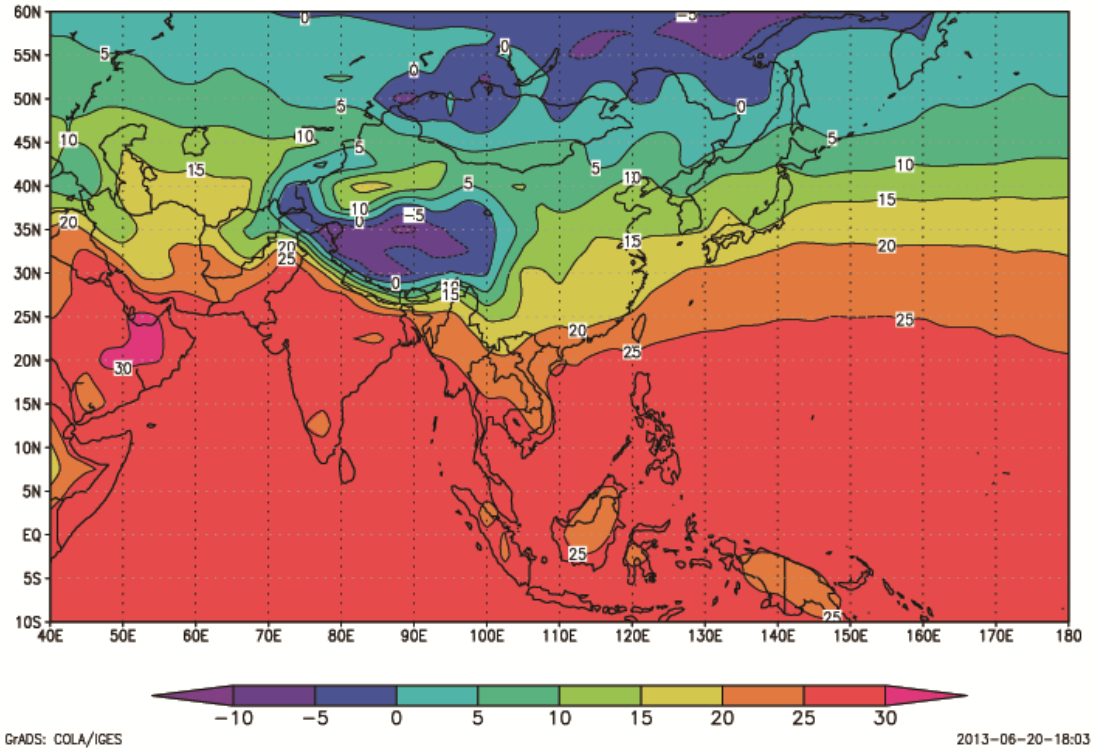

Fig. SE4a. Composite surface air temperature (SAT) for the five years (July to June) with highest precipitation as represented in the 6-site average series (1959, 1978, 1989, 1999 and 2010), here using the NCEP/NCAR reanalysis dataset. In this and the following cases, the highest and lowest precipitation years are identified in each of the five 11-year periods 1957-1967, 1968-1978, 1979-1989, 1990-2000 and 2001-2011 for the purpose of avoiding the effect of trend on the final results.

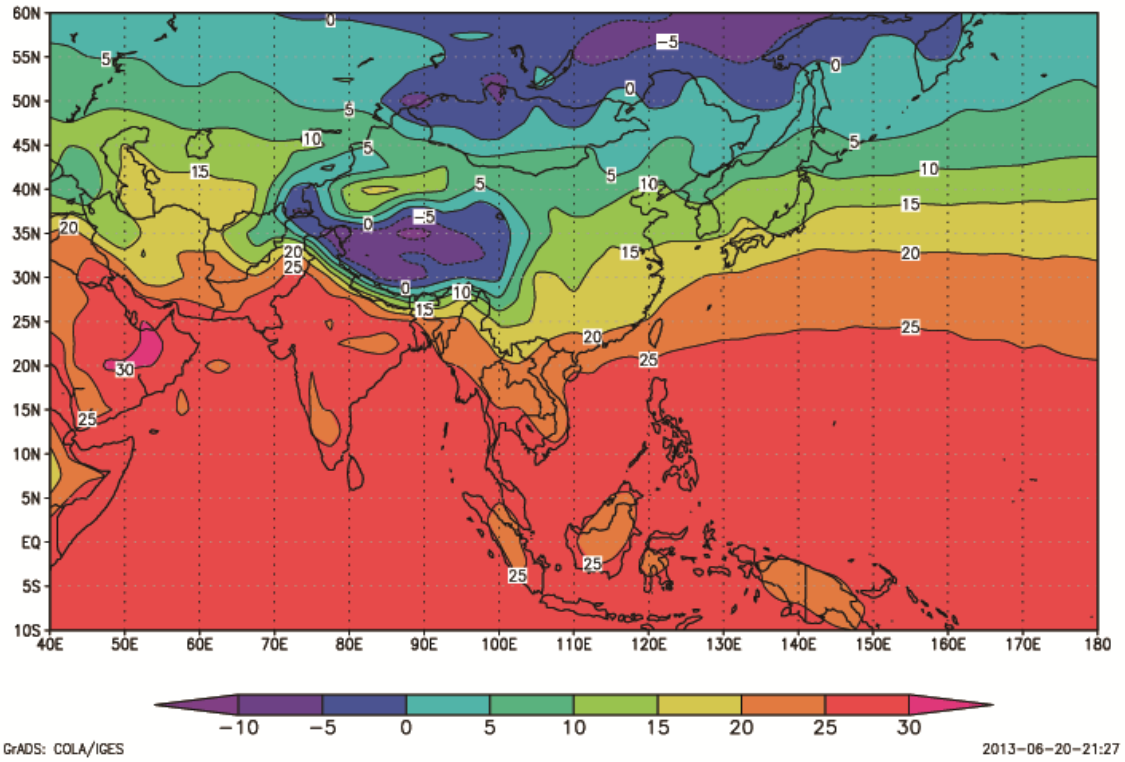

Fig. SE4b. As for 4a but showing the field for the 5 years of lowest precipitation (1957, 1971, 1979, 1995 and 2001).

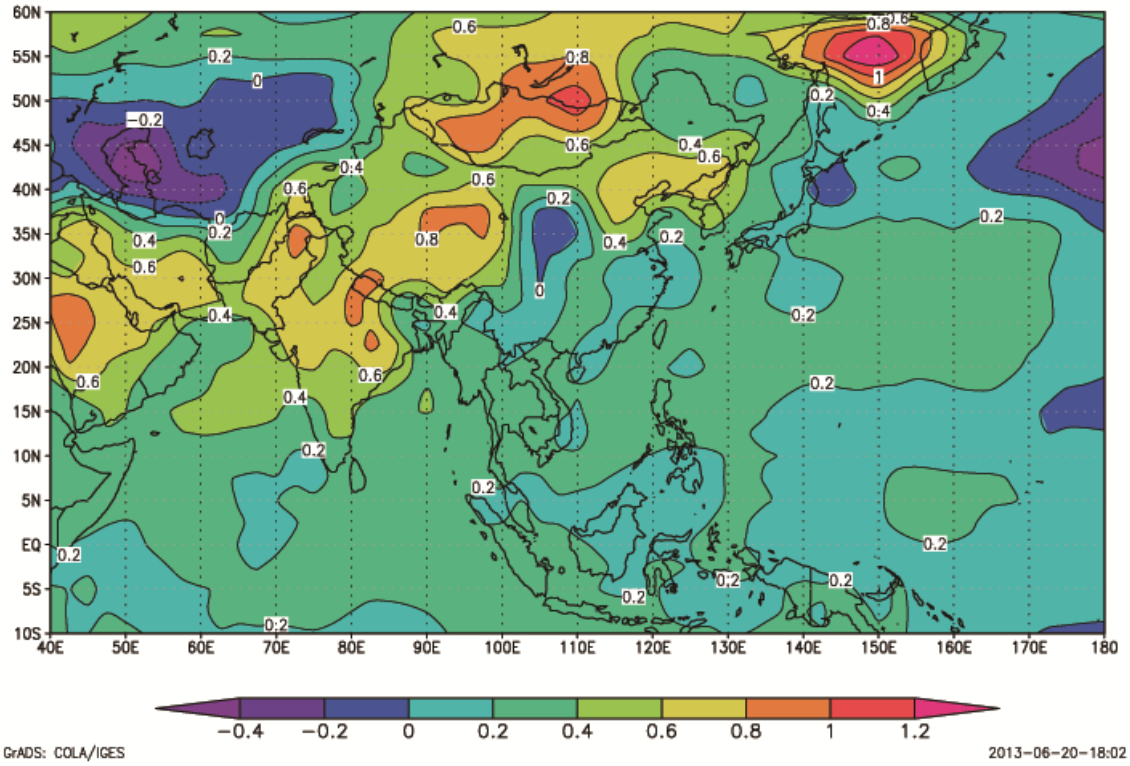

Fig. SE4c. The difference in annual SAT (July-June) between years with highest and lowest precipitation.

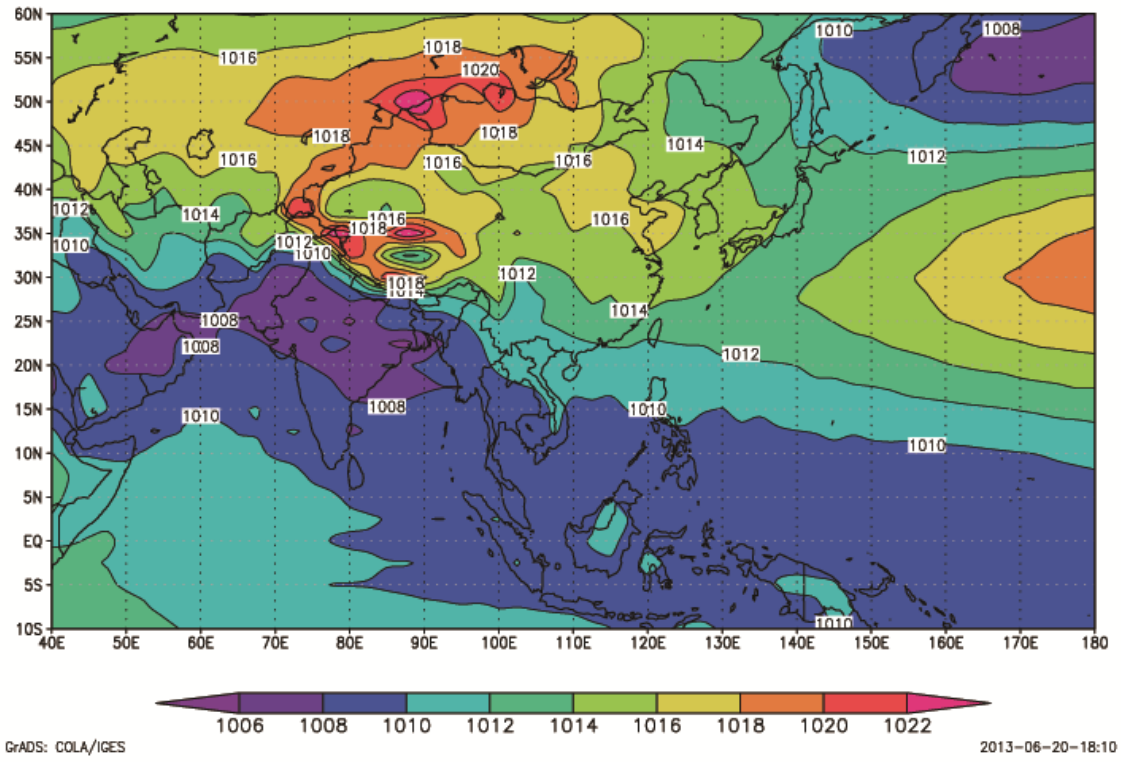

Fig. SE5a. Composite Sea level pressure (SLP) in July-June for the five years with highest precipitation (1959, 1978, 1989, 1999 and 2010) based on the NCEP/NCAR dataset.

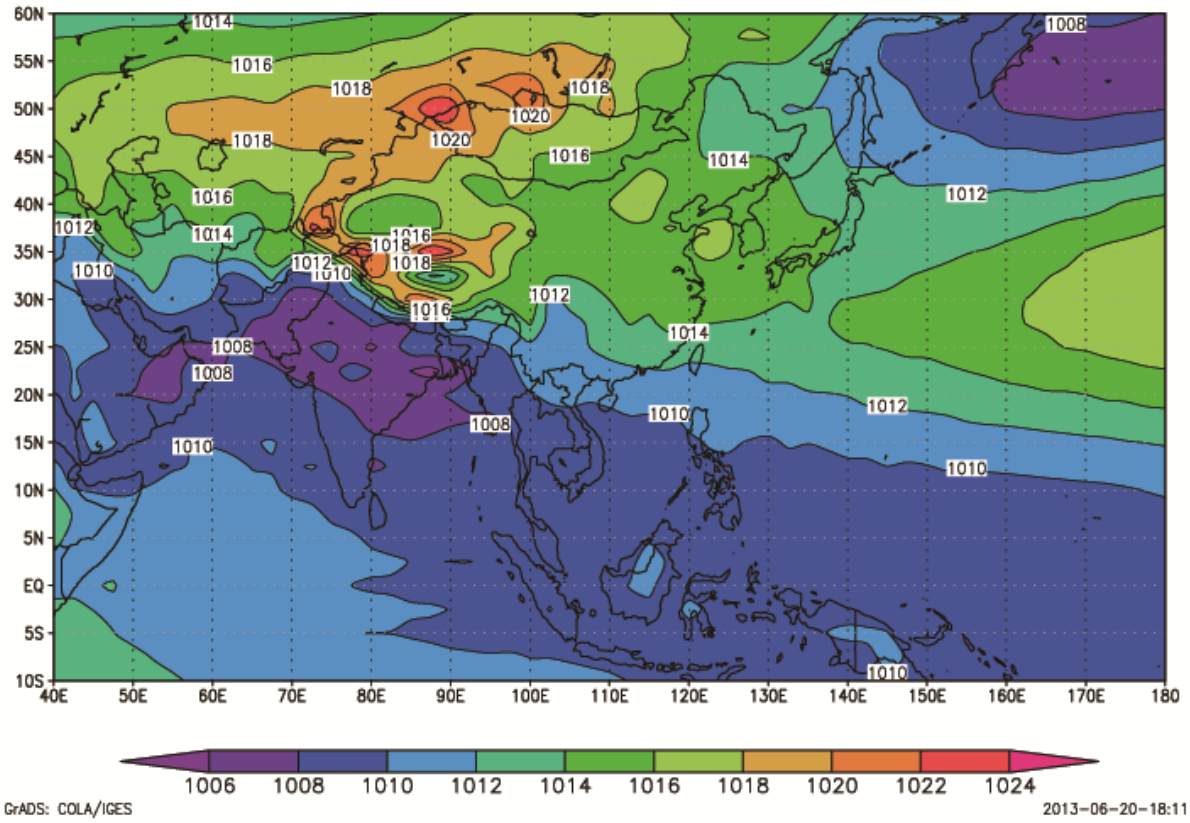

Fig. SE5b. As for 5a but showing the SLP pattern based on the five years with lowest precipitation (1957, 1971, 1979, 1995 and 2001).

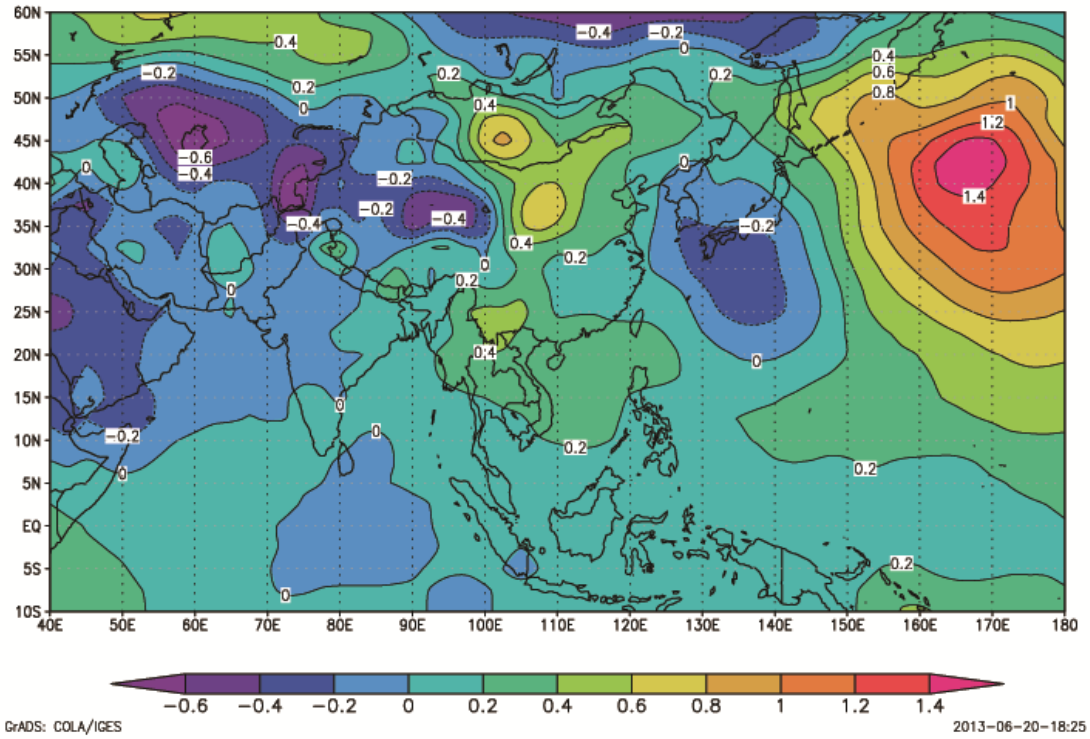

Fig. SE5c. The difference in annual SLP (July-June) for the years with highest and lowest precipitation.

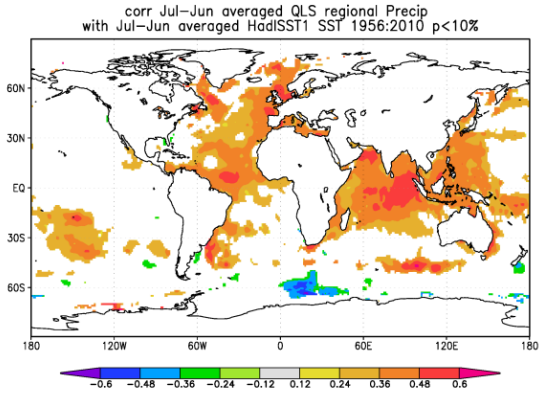
corr Jul–Jun averaged QLS regional Precip
with Jul–Jun averaged HadISST1 SST 1956:2010 p<10%
60N
30N
EQ
30S
60S
180
120W
60W
0
60E
120E
180
−0.6 −0.48 −0.36 −0.24 −0.12 0.12 0.24 0.36 0.48 0.6

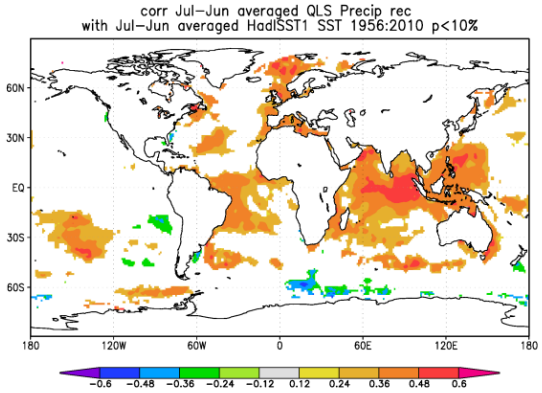
corr Jul–Jun averaged QLS Precip rec
with Jul–Jun averaged HadISST1 SST 1956:2010 p<10%
60N
30N
EQ
30S
60S
180
120W
60W
0
60E
120E
180
−0.6 −0.48 −0.36 −0.24 −0.12 0.12 0.24 0.36 0.48 0.6

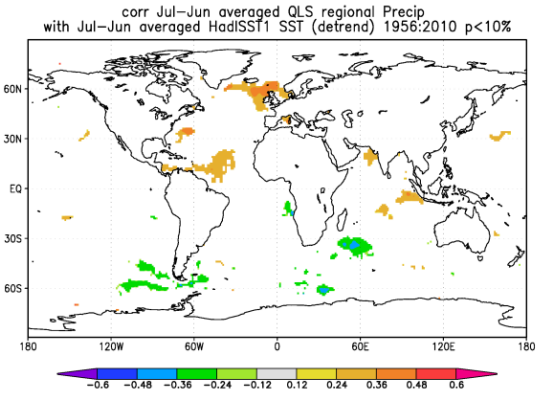
corr Jul–Jun averaged QLS regional Precip
with Jul–Jun averaged HadISST1 SST (detrend) 1956:2010 p<10%
60N
30N
EQ
30S
60S
180
120W
60W
0
60E
120E
180
−0.6 −0.48 −0.36 −0.24 −0.12 0.12 0.24 0.36 0.48 0.6

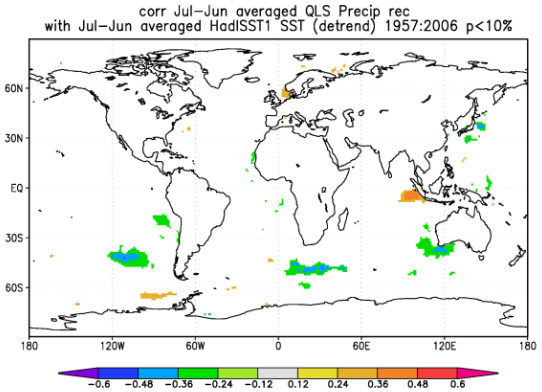
corr Jul–Jun averaged QLS Precip rec
with Jul–Jun averaged HadISST1 SST (detrend) 1957:2006 p<10%
60N
30N
EQ
30S
60S
180
120W
60W
0
60E
120E
180
−0.6 −0.48 −0.36 −0.24 −0.12 0.12 0.24 0.36 0.48 0.6

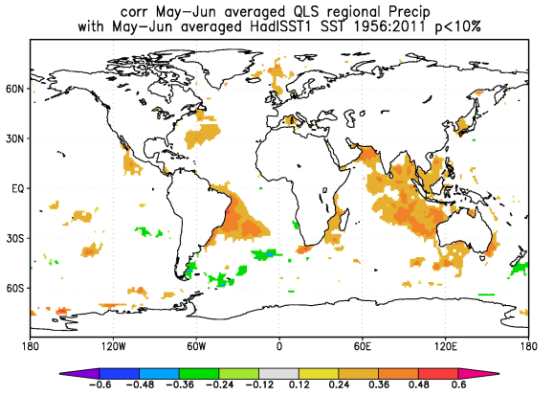
corr May–Jun averaged QLS regional Precip
with May–Jun averaged HadISST1 SST 1956:2011 p<10%
60N
30N
EQ
30S
60S
180
120W
60W
0
60E
120E
180
−0.6 −0.48 −0.36 −0.24 −0.12 0.12 0.24 0.36 0.48 0.6

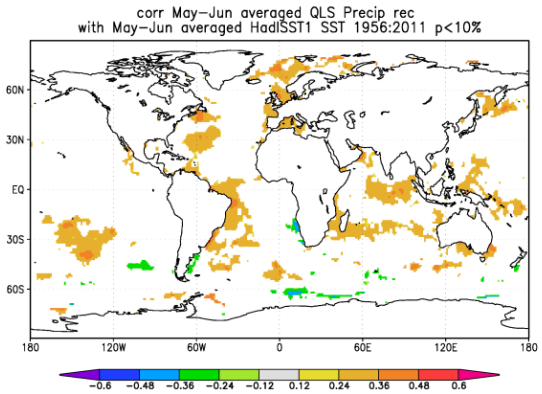
corr May–Jun averaged QLS Precip rec
with May–Jun averaged HadISST1 SST 1956:2011 p<10%
60N
30N
EQ
30S
60S
180
120W
60W
0
60E
120E
180
−0.6 −0.48 −0.36 −0.24 −0.12 0.12 0.24 0.36 0.48 0.6

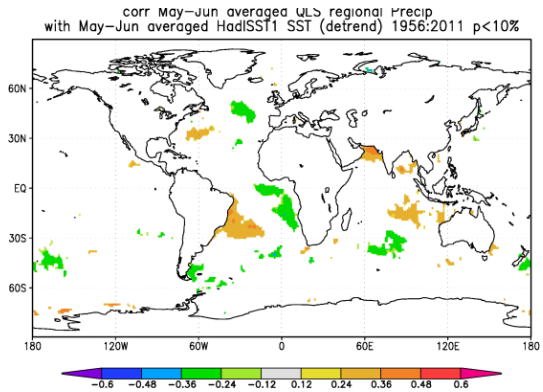
corr May–Jun averaged QLS regional Precip
with May–Jun averaged HadISST1 SST (detrend) 1956:2011 p<10%
60N
30N
EQ
30S
60S
180
120W
60W
0
60E
120E
180
−0.6 −0.48 −0.36 −0.24 −0.12 0.12 0.24 0.36 0.48 0.6

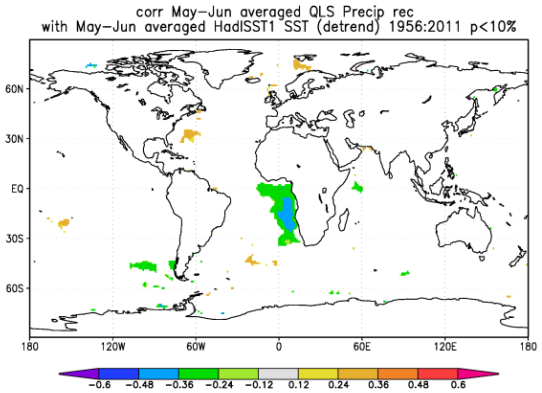
corr May–Jun averaged QLS Precip rec
with May–Jun averaged HadISST1 SST (detrend) 1956:2011 p<10%
60N
30N
EQ
30S
60S
180
120W
60W
0
60E
120E
180
−0.6 −0.48 −0.36 −0.24 −0.12 0.12 0.24 0.36 0.48 0.6

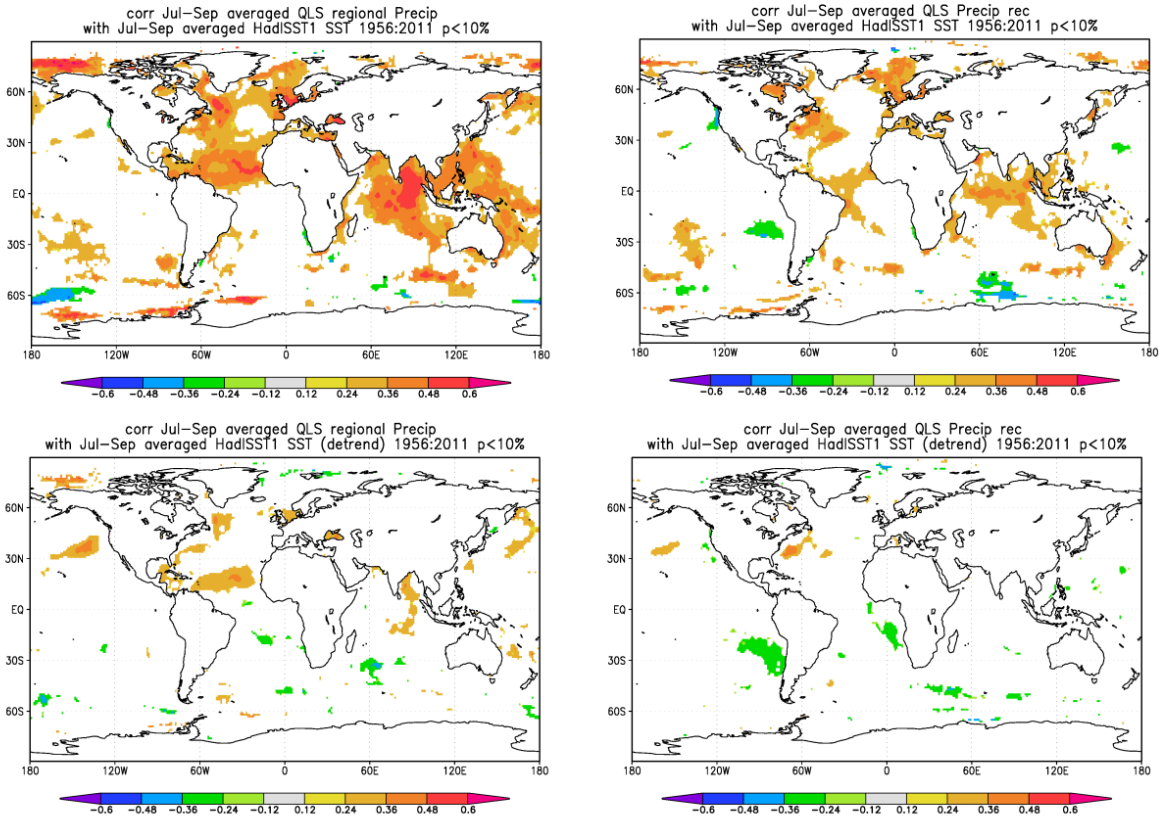

Fig. SE6. Patterns of correlation between the observed regional precipitation series for the study region and concurrent observed global SSTs (from HadiSST1). Maps show annual average values (July to June); May to June; and July to September seasons. Maps based on mutually detrended records are also shown.

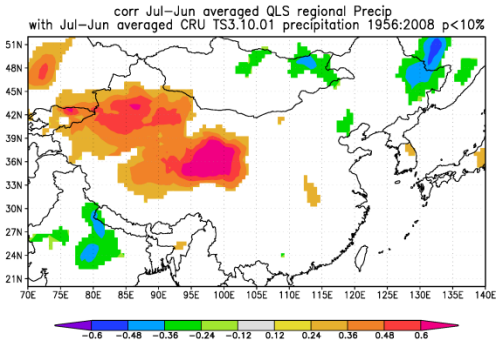
corr Jul–Jun averaged QLS regional Precip
with Jul–Jun averaged CRU TS3.10.01 precipitation 1956:2008 p<10%

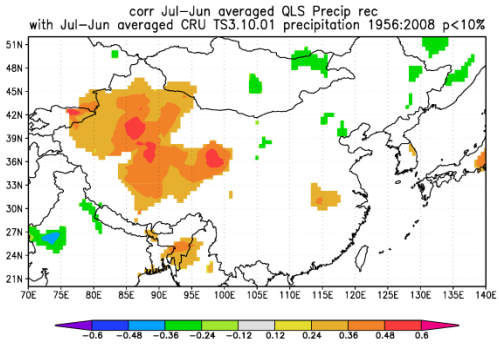
corr Jul–Jun averaged QLS Precip rec
with Jul–Jun averaged CRU TS3.10.01 precipitation 1956:2008 p<10%

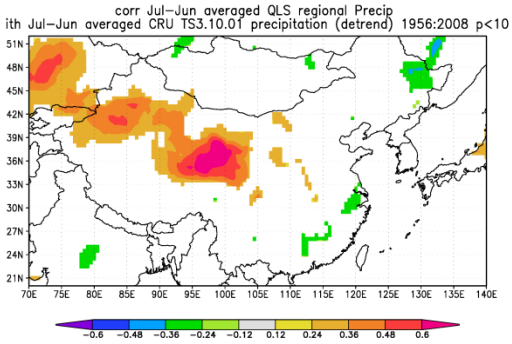
corr Jul–Jun averaged QLS regional Precip
ith Jul–Jun averaged CRU TS3.10.01 precipitation (detrend) 1956:2008 p<10

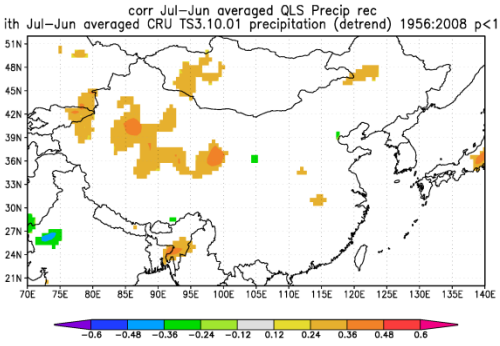
corr Jul–Jun averaged QLS Precip rec
ith Jul–Jun averaged CRU TS3.10.01 precipitation (detrend) 1956:2008 p<10

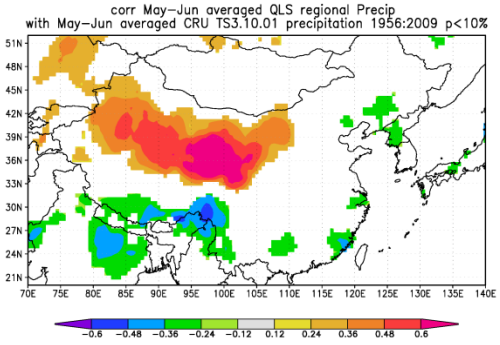
corr May–Jun averaged QLS regional Precip
with May–Jun averaged CRU TS3.10.01 precipitation 1956:2009 p<10%

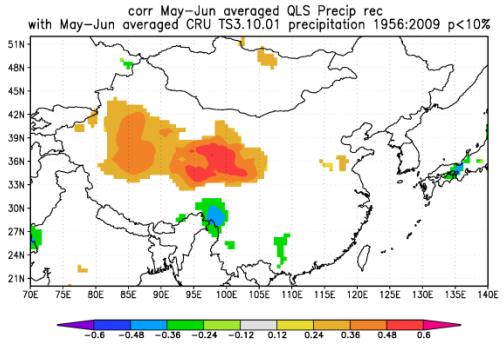
corr May–Jun averaged QLS Precip rec
with May–Jun averaged CRU TS3.10.01 precipitation 1956:2009 p<10%

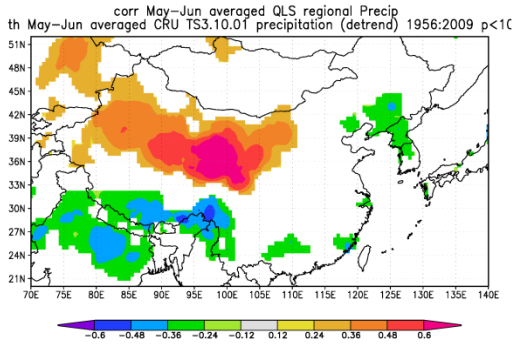
corr May–Jun averaged QLS regional Precip
th May–Jun averaged CRU TS3.10.01 precipitation (detrend) 1956:2009 p<1

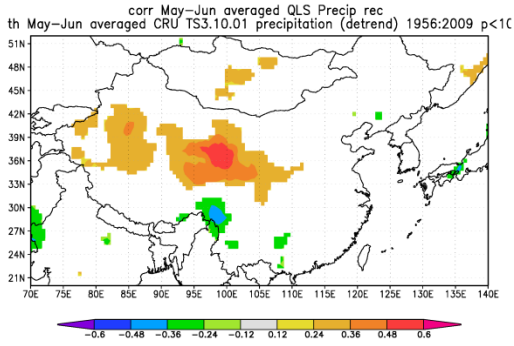
corr May–Jun averaged QLS Precip rec
th May–Jun averaged CRU TS3.10.01 precipitation (detrend) 1956:2009 p<1

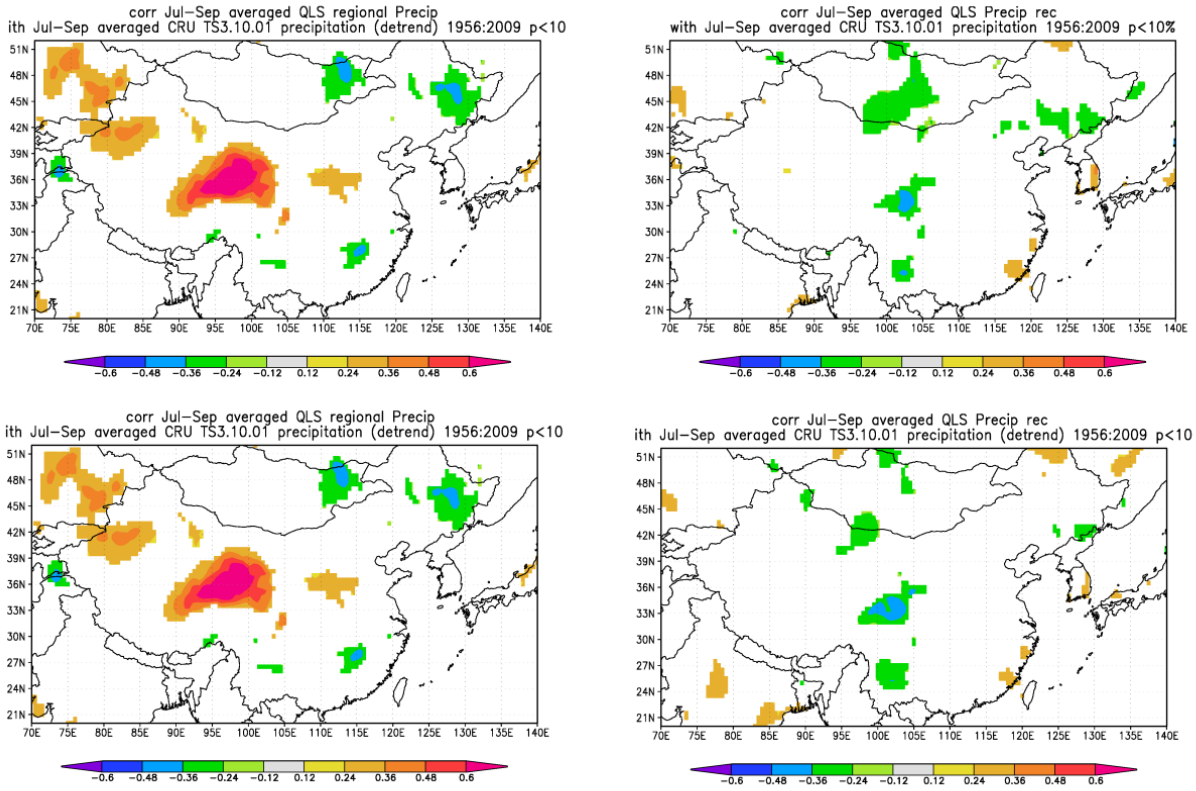

Fig. SE7. Patterns of correlation between the observed regional precipitation series for the study region and observed precipitation from the Climatic Research Unit TS 3.10.01 (land) 0.5 º gridded dataset using measured and mutually detrended data.

Table SE1. Wettest and driest periods. Ten estimated wettest and ten driest periods of length 1, 10, 25, 50 and 100 years from the precipitation reconstruction since 1500 BCE. The central estimate ±2 standard errors (mm) of the reconstructed annual precipitation are given in each case, even during the instrumental period. Where the indicated error range would yield values less than zero, they should be truncated at zero. The regression was calibrated against the instrumental record, with annual precipitation ranging from 162 to 427 mm, and therefore estimates of the precipitation amounts in very dry years/periods should be treated with caution because they represent extrapolations outside the calibration range. Negative years refer to the astronomical calendar (including year 0), so that –1347 is equivalent to 1348 BCE.

Timescale	1 year		10 years		25 years		50 years		100 years	
Rank	mm	Year	mm	Years	mm	Years	mm	Years	mm	Year
Wettest										
1	399 ±63	2010	319 ±29	2002:2011	278 ±29	1987:2011	258 ±28	1962:2011	242 ±30	579: 678
2	334 ±62	2006	273 ±28	1985:1994	258 ±28	970: 994	248 ±30	604: 653	240 ±28	888: 987
3	334 ±63	2009	271 ±41	–903:–894	254 ±40	–914:–890	242 ±28	964:1013	239 ±28	1912:2011
4	331 ±64	2011	268 ±28	971: 980	253 ±30	602: 626	241 ±29	888: 937	229 ±40	–983:–884
5	323 ±62	2005	267 ±27	1574:1583	252 ±29	921: 945	240 ±39	–933:–884	226 ±29	788: 887
6	317 ±62	2002	264 ±29	888: 897	251 ±30	633: 657	233 ±29	806: 855	226 ±27	1312:1411
7	313 ±62	974	263 ±29	928: 937	250 ±29	876: 900	233 ±27	1534:1583	221 ±27	1517:1616
8	311 ±72	–1347	263 ±39	–948:–939	245 ±27	1886:1910	230 ±27	1314:1363	221 ±28	992:1091
9	309 ±62	585	263 ±28	983: 992	243 ±44	–1483:–1459	230 ±41	–1487:–1438	216 ±27	1809:1908
10	309 ±62	1999	261 ±30	602: 611	243 ±27	1559:1583	228 ±27	1862:1911	213 ±31	684: 783
Driest										
1	4 ±70	–1049	118 ±29	–206:–197	146 ±28	353: 377	158 ±31	–388:–339	172 ±31	–435:–336
2	27 ±62	1824	121 ±28	366: 375	147 ±30	–219:–195	162 ±27	1450:1499	176 ±28	278: 377
3	31 ±63	–383	138 ±31	–593:–584	152 ±31	–388:–364	163 ±30	–230:–181	178 ±39	–1147:–1048
4	32 ±64	–586	142 ±42	–1251:–1242	161 ±27	1449:1473	165 ±28	328: 377	180 ±27	1630:1729
5	32 ±62	–200	142 ±28	115: 124	161 ±31	–608:–584	168 ±31	–633:–584	180 ±31	–659:–560
6	43 ±62	360	143 ±27	1450:1459	162 ±27	1475:1499	172 ±31	–508:–459	182 ±27	1421:1520
7	48 ±61	1495	144 ±41	–1054:–1045	163 ±28	114: 138	173 ±27	1684:1733	182 ±31	–547:–448
8	49 ±68	–961	145 ±31	–349:–340	164 ±42	–1211:–1187	175 ±39	–1149:–1100	183 ±30	–226:–127
9	52 ±70	–1242	145 ±27	1476:1485	164 ±31	–363:–339	176 ±28	261: 310	183 ±28	45: 144
10	58 ±66	–725	147 ±31	–373:–364	164 ±27	1693:1717	177 ±28	89: 138	185 ±29	–70: 29

Comparison of wet periods. The standard error of the difference between two precipitation means, X and Y, is $SE = \sqrt{(SE_X^2 + SE_Y^2)}$ where SE_X and SE_Y are the standard errors of the two means (note that in Table SE1, the values shown are ±2 standard errors incorporating both chronology and interpretational uncertainty). For means that are normally distributed, the probability that $X > Y$ exceeds 66% if $(X - Y) / SE > 0.42$ for a one-tailed test (i.e., when there is an *a priori* expectation that period X may be wetter). For a two-tailed test, the ratio would need to exceed 0.96, and for greater probability (i.e., higher confidence) the ratio would need to be higher still.

The ratios of the difference between the wettest and second wettest (non-overlapping) periods and the respective difference standard errors are 1.46 (1-year), 2.26 (10-year), 0.99 (25-year), 0.46 (50-year) and 0.13 (100-year). For each of the averaging periods from 1 to 50 years in length, therefore, the wettest period in the reconstructions (always in the recent, instrumental period) is likely wetter than the second wettest period. The ratio (and therefore the confidence) is lower for the 50-year means, where the difference between the 1962–2011 and 604–653 means is only 10 mm (though this is still a significant proportion of the overall range from the entire 3500-year reconstruction, which is only 100 mm between the driest and wettest 50-year means). Note also that we have not included any reduction in the uncertainty range of reconstructed 50-year means compared with 10-year means. This is the basis for our assessment that the wettest 50-year period in the last 3500 years is "likely" to be the most recent in the record, i.e. 1962–2011.

Section F: exploring and quantifying QLS chronology uncertainty

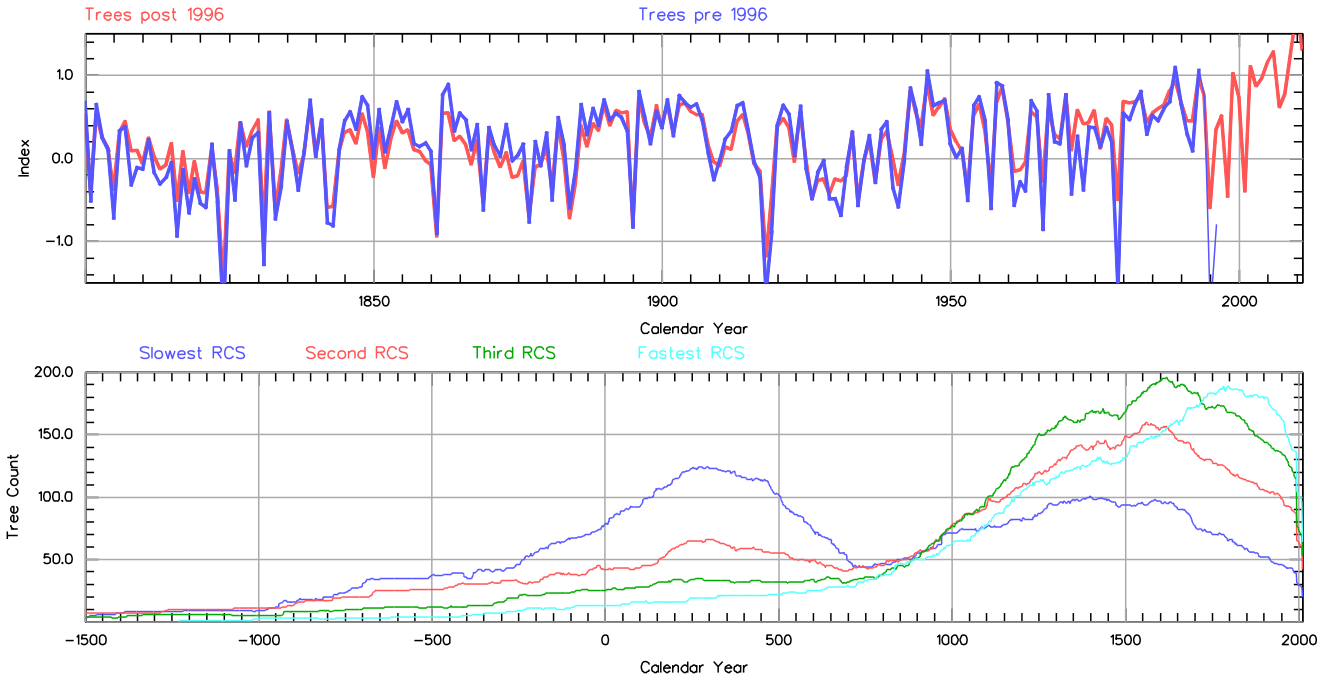

Fig. SF1. A chronology was created using four-curve SF RCS with tree indices transformed to have a normal distribution. Indices from trees ending after 1996 were averaged into a chronology and all other tree indices were averaged into a separate chronology. The two chronologies are plotted in the upper panel and show that the trees ending before 1996 do not have a different signal to those ending after 1996. The lower plot shows the changing counts of trees in each RCS curve through time. The fastest growing tree counts peak in the period 1700-1900. The older (slower growing trees) have highest counts in the period 200 to 400.

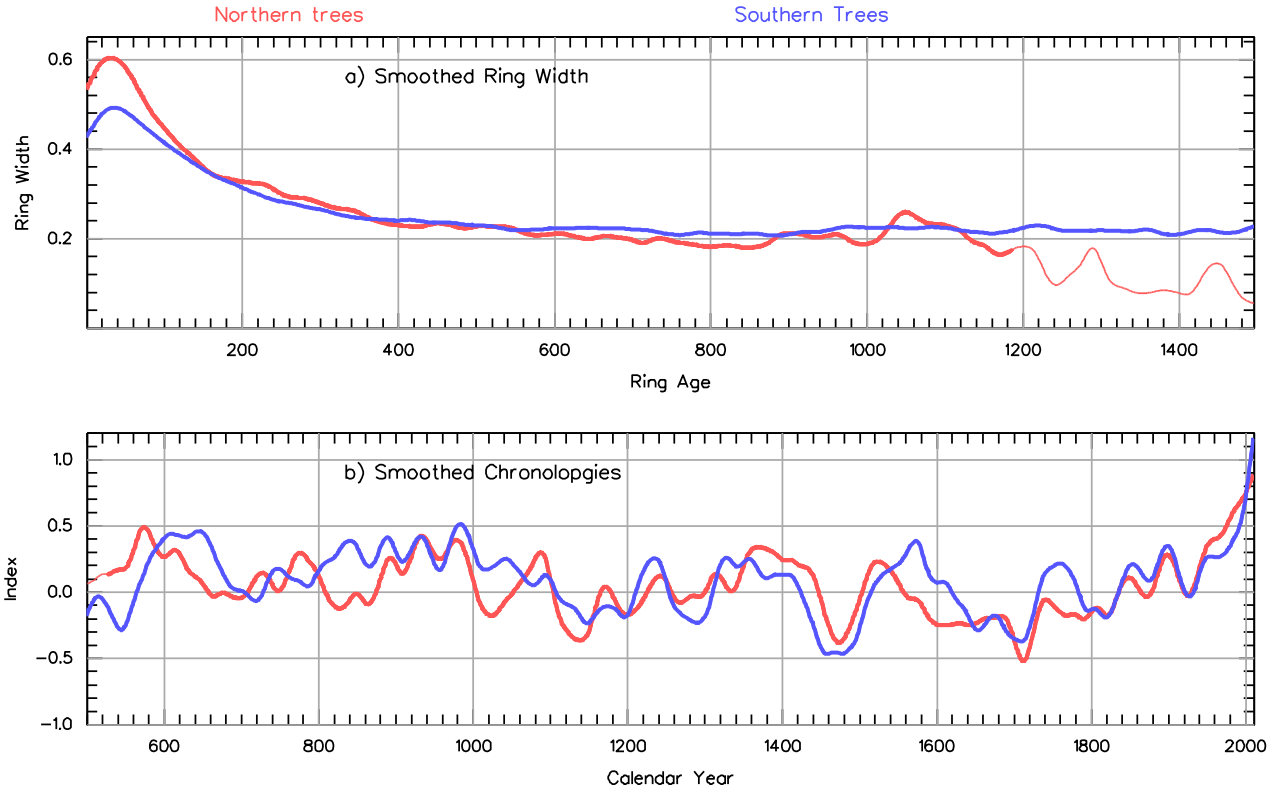

Fig. SF2. A chronology was created using four-curve SF RCS with tree indices transformed to have a normal distribution. Separate means of signal-free measurements (a) and tree indices (b) were calculated for the northern sites (HYG and ZMSX) and the southern sites (DLH, GM, Dulan, Chin005 and Chin006) in order to highlight any differences and potential regional bias. Series were smoothed with a 50- year spline. Thin lines are used where sample counts are below 6. The northern trees (red) show a slightly higher juvenile growth rate during their first century than do the southern trees (blue). There is general agreement in the multi-centennial variability of both chronologies but some discrepancies at multi-decadal periods.

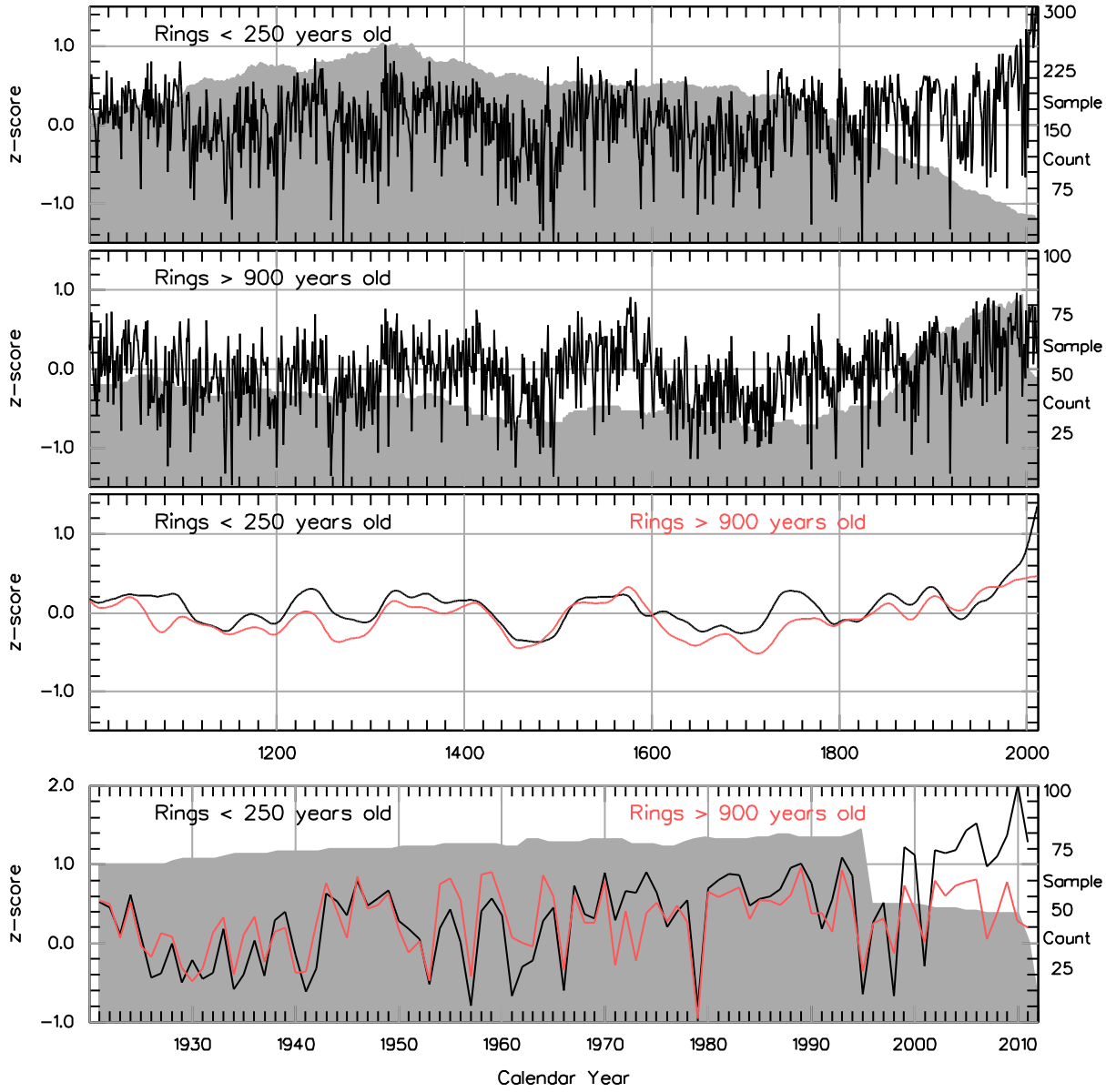

Fig. SF3 Comparison of the means of indices from young rings and old rings. A chronology was created using four-curve SF RCS with tree indices transformed to have a normal distribution. The mean of tree-ring indices for rings that grew before the tree was 250 years old (young rings) and rings that grew after the tree was 900 years old (old rings) were separately calculated and the values of the last millennium are plotted by calendar year in the upper two panels. The third panel shows these chronologies after 50-year low-pass smoothing. The most recent 90 years are plotted in the lowest panel to highlight when the signals separate. Sample counts are shown with grey shading.

Figures SA5 and SA6 show examples of trees with strip-bark growth form showing that for the first few centuries trees tend to be circular while in later centuries growth ceases in many directions and is concentrated in a few directions only. Figure SF3 was developed to test the hypothesis that when living strip-bark trees are sampled the sampling process is biased towards the direction showing most growth in the years prior to samples being taken and as a result the growth rate of strip bark trees might be higher in the most recent century than the growth rate of trees with a

circular growth form. Here the young rings will be predominately circular growth form while the old rings will be mainly strip bark growth form. The two chronologies (3rd panel) are very similar over the last 1000 years indicating a lack of systematic bias between the different growth forms. The young rings showing an increase in recent decades relative to old rings and this is shown to be a step increase from the late 1990s contradicting the possibility of a 'strip bark' growth enhancement in recent years. This increase coincides with changes in the site make up of the regional chronology (note change in old rings sample counts around 1998) and is dependent on the years in which each site was sampled. The very recent increase in the "young rings" subsample reflects the makeup of this section of the chronology, when the majority of measurements are from the MNT site which is located in the drier "southern" region (Figure 1) where the relative rainfall increase has been greater than that in the wetter "northern" region (Figure SA1).

"Adjusted" EPS as an alternative indicator of full-spectrum chronology uncertainty

In the following Figs. (SF4-6) all trees were standardised firstly with a 200-year high-pass spline and secondly with RCS using four-curve SF RCS with tree indices converted to have a normal distribution. The top panel shows the running Rbar (using a 200-year window) for the spline (black) and RCS (red) chronologies. The RCS chronology, which retains more low frequency than the spline chronology, has lower Rbar values as expected. The traditional EPS was calculated and is plotted in the lower panel for the spline (black) and RCS (green) chronologies. The EPS is slightly lower for the RCS chronology due to the lower Rbar. This EPS calculation removes long timescale variance (the 200-year high- pass filtering effect of using a running window for Rbar calculations) and is suitable for the spline chronology, but for the RCS chronology the EPS calculation does not account for low-frequency variance between trees and considerably over-estimates chronology strength. To allow for the low-frequency variance an "effective count" is estimated using the standard deviations of spline and RCS chronologies (i.e. the count needed to reduce the low-frequency scatter to that evident in the spline chronology). The count in each year was reduced by dividing by the squared ratio of the mean standard deviations (mean RCS standard deviation divided by mean spline standard deviation calculated over a 200-year window). This effective count is used to calculate an adjusted EPS for the RCS chronologies shown in Figs SF4 to SF6 (see ref. 2, SM6 Part EC3 and ref. 18 in the main text for further details of this method).

Note the change in the strength of common chronology signal represented by the fall in Rbar and EPS pre-and post- circa 550 CE in the final chronology (SF6). The higher earlier Rbar values largely offset the effect of reducing sample size which would otherwise reduce the EPS. However, some caution is warranted here because the higher earlier Rbar values reflect a more local origin of the constituent samples compared to the increasing wider geographical origin of the samples post 550 CE. Nevertheless, comparison of two chronologies representing "northern" and "southern" region trees (over the overlap period circa 550 CE onwards) confirms a general pattern of common chronology variability in these data (see SI Fig. SF2, SF4 and SF5).

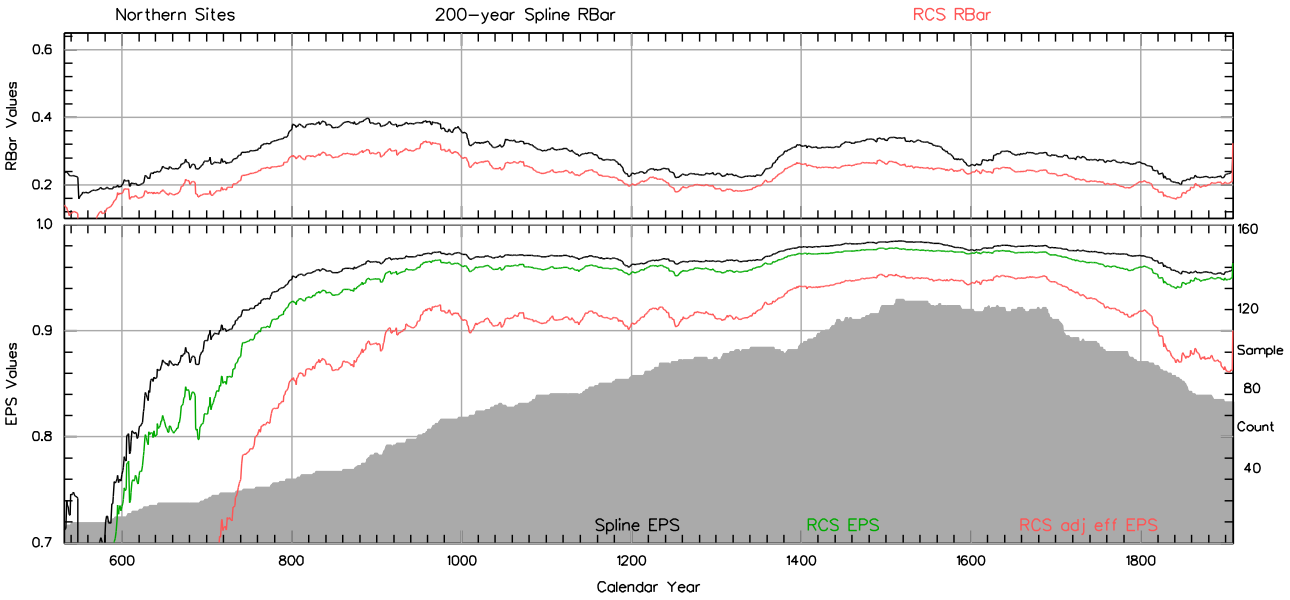

Fig. SF4. The adjusted EPS was calculated using the data from the northern sites (HYG and ZMSX) and is shown in the lower panel. The EPS remains above 0.9 for most of the period of the chronology and drops below 0.85 prior to 800 CE.

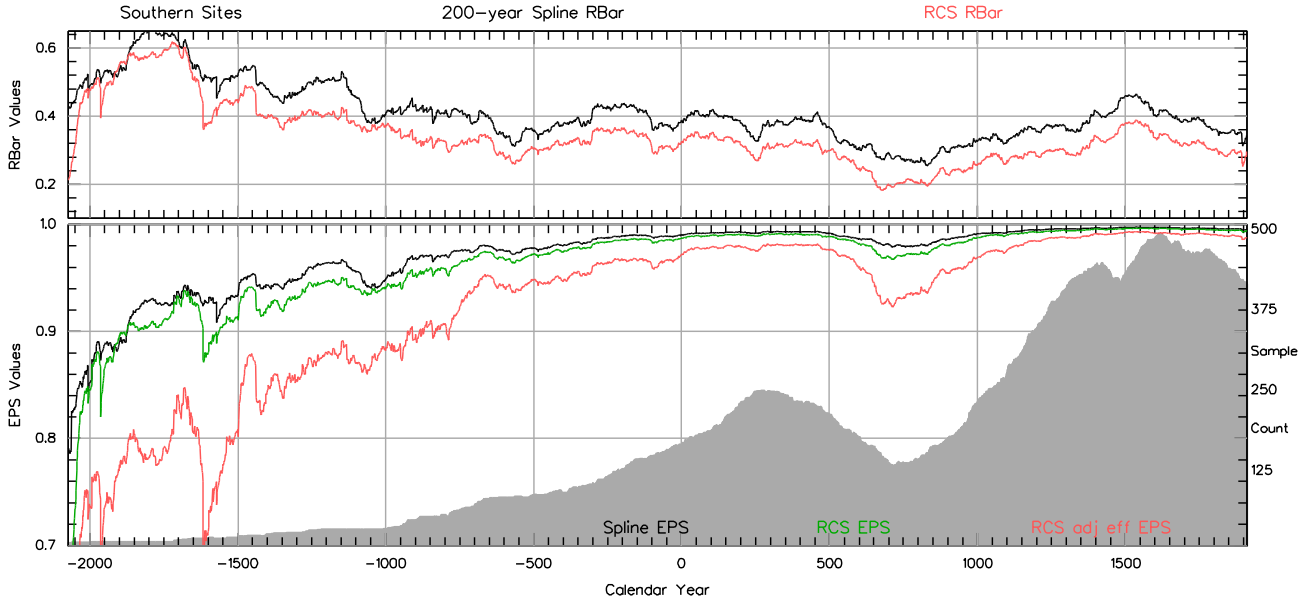

Fig. SF5. The adjusted EPS was calculated using the data from the southern sites (DLH, GM, Dulan, Chin005 and Chin006) and is shown in the lower panel. The EPS remains above 0.9 back to 800 BCE and drops below 0.85 prior to 1500 BCE.

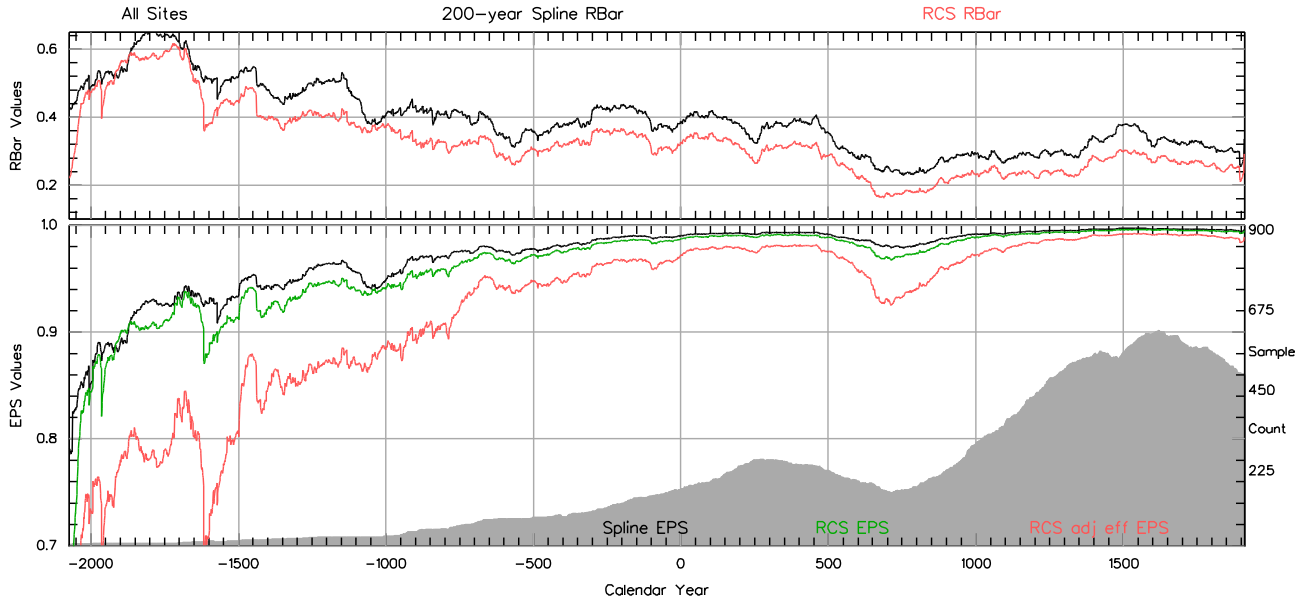

Fig. SF6. The adjusted EPS was calculated using all data for all sites and is shown in the lower panel. Rbar is not noticeably different during the period when data from northern and southern sites are combined (800 CE to present). The EPS remains above 0.9 back to 800 BCE and drops below 0.85 prior to 1500 BCE. Compare these EPS values with the uncertainty represented by the 2 standard errors of the index data shown in SF7.

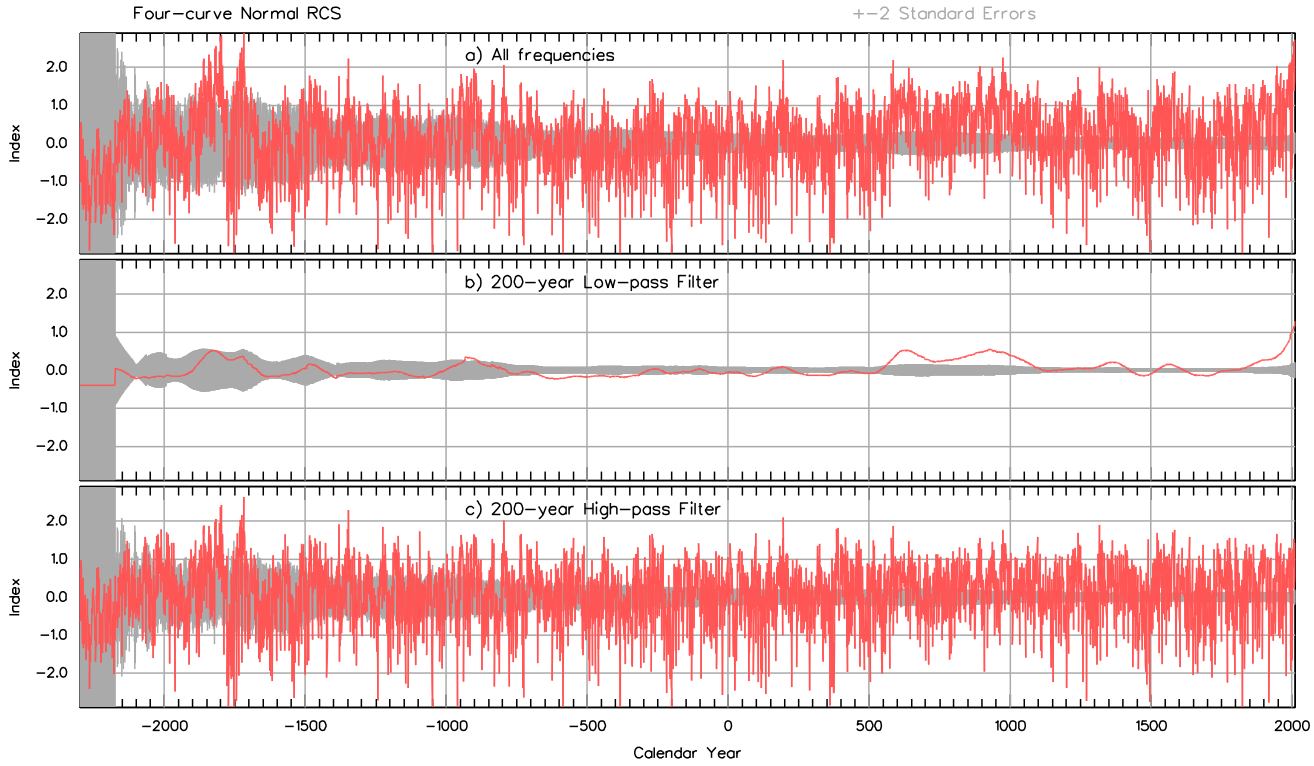

Fig. SF7. A chronology was created using four-curve SF RCS with tree indices transformed to have a normal distribution. Series of low-pass tree indices were created by smoothing the data from each tree with a 200-year spline. High-pass indices were created by subtracting the low-pass indices from the original indices. The three sets of indices were averaged into three separate chronologies (all frequencies, 200-year high pass and 200-year low pass) and in each case the 2 standard error values were calculated for each year with >3 trees. These errors were calculated as 2 standard deviations scaled by the square root of the tree count. The full chronology was rescaled by subtracting the mean and dividing by the standard deviation. The low and high-pass chronologies have each had their mean removed and were then also divided by the full chronology standard deviation. The full (top), 200-year low pass (centre) and 200-year high pass chronologies are shown below with their 2 standard error bars plotted (as grey shading) either side of zero.

Section G: comparison of QLS inferred precipitation and various temperature reconstructions

Table SG1. Correlations between the QLS TRW chronology and large scale hemispheric/global temperature reconstructions as listed in Table 5 A6 of ref. 13.

	Overlap			Correlations			Ref.
Global							
Temperature recon.	Years	Start	End	raw	<30yr	>30yr	
Leclercq (2012)	401	1600	2000	0.32	-0.00	0.61	(14)
Mann (2008) eiv_GLC	1507	500	2006	0.26	-0.03	0.5	(15)
Mann (2008) eiv_GLH	1507	500	2006	0.29	-0.01	0.56	(15)
Instrumental Temperature							
hadcrut4_gl Morice (2012)	162	1850	2011	0.34	-0.07	0.62	(16)
crutem4_gl Jones (2012)	161	1851	2011	0.38	0.02	0.64	(17)
Southern Hemisphere							
Temperature recon.	Years	Start	End	raw	<30yr	>30yr	
Leclercq (2012)	401	1600	2000	0.32	-0.07	0.63	(14)
Mann (2008) cps_SHC	1496	500	1995	0.15	0.06	0.28	(15)
Mann (2008) eiv_SHC	1807	200	2006	0.25	0	0.49	(15)
Mann (2008) eiv_SHH	1607	400	2006	0.25	-0.01	0.48	(15)
Instrumental Temperature							
hadcrut4_sh Morice (2012)	162	1850	2011	0.32	-0.08	0.62	(16)
crutem4_sh Jones (2012)	161	1851	2011	0.29	-0.02	0.63	(17)
Northern Hemisphere (series incorporated in our NH composite)							
Temperature recon.	Years	Start	End	raw	<30yr	>30yr	
Frank (2007)	1162	831	1992	0.25	0.06	0.47	(18)
Moberg (2005)	1979	1	1979	0.12	0	0.29	(19)
D'Arrigo (2006) scaled	1283	713	1995	0.2	-0.03	0.48	(5) in the main text
Hegerl (2007)	1403	558	1960	0.2	-0.01	0.4	(2) in the main text
Ljungqvist (2010) decadal	1999	1	1999	0.16	0.02	0.31	(20)
Juckes (2007) cvm	981	1000	1980	0.21	0.07	0.42	(21)
Christiansen (2012)	1973	1	1973	0.16	0.01	0.33	(22)
Loehle (2008)	1920	16	1935	0.2	0.01	0.39	(23)
Mann (2009) fullNH	1507	500	2006	0.27	0.03	0.51	(24)
Mann (2008) minus7_e	1508	500	2007	0.28	0	0.55	(15)
Shi (2013) NHtemp_	999	1000	1998	0.29	0.11	0.56	(25)
Other reconstructions not used in the NH composite							
Temperature recon.	Years	Start	End	raw	<30yr	>30yr	
Leclercq (2012)	401	1600	2000	0.21	-0.02	0.36	(14)
Ammann (2007)	981	1000	1980	0.11	0.03	0.26	(26)
Briffa (2001)	559	1402	1960	0.12	0.1	0.19	(27)
Mann (2008) cps_NHC	1796	200	1995	0	0	-0.02	(15)
Mann (2008) eiv_NHC	1707	300	2006	0.2	-0.04	0.38	(15)
Mann (2008) eiv_NHH	1707	300	2006	0.24	0	0.45	(15)
Instrumental							
hadcrut4_nh Morice (2012)	162	1850	2011	0.34	-0.05	0.6	(16)
hadcrut4 Morice (2012)	162	1850	2011	0.37	0.06	0.6	(16)
crutem4_nh Jones (2012)	162	1850	2011	0.38	0.03	0.64	(17)
crutem4 Jones (2012)	162	1850	2011	0.38	0.06	0.63	(17)

Table SG1. (continued) NH composite

Reference period (max common): 1007 to 1928					Correlation
NH	composite	1969	23	1991	(30-yr low-pass): 0.45
NH	composite	1479	507	1985	30-yr low-pass): 0.58
Reference period (max common): 1119 to 1816					
NH	composite	1745	135	1879	(30-500-yr band-pass): 0.41
NH	composite	1255	619	1873	(30-500-yr band-pass): 0.42
Reference period (max common): 1024 to 1911					
NH	composite	1935	40	1974	(30-100-yr band-pass): 0.15
NH	composite	1445	524	1968	(30-100-yr band-pass): 0.27
Reference period (max common): 1119 to 1816					
NH	composite	1745	135	1879	(100-500-yr band-pass) 0.53
NH	composite	1255	619	1873	(100-500-yr band-pass) 0.49

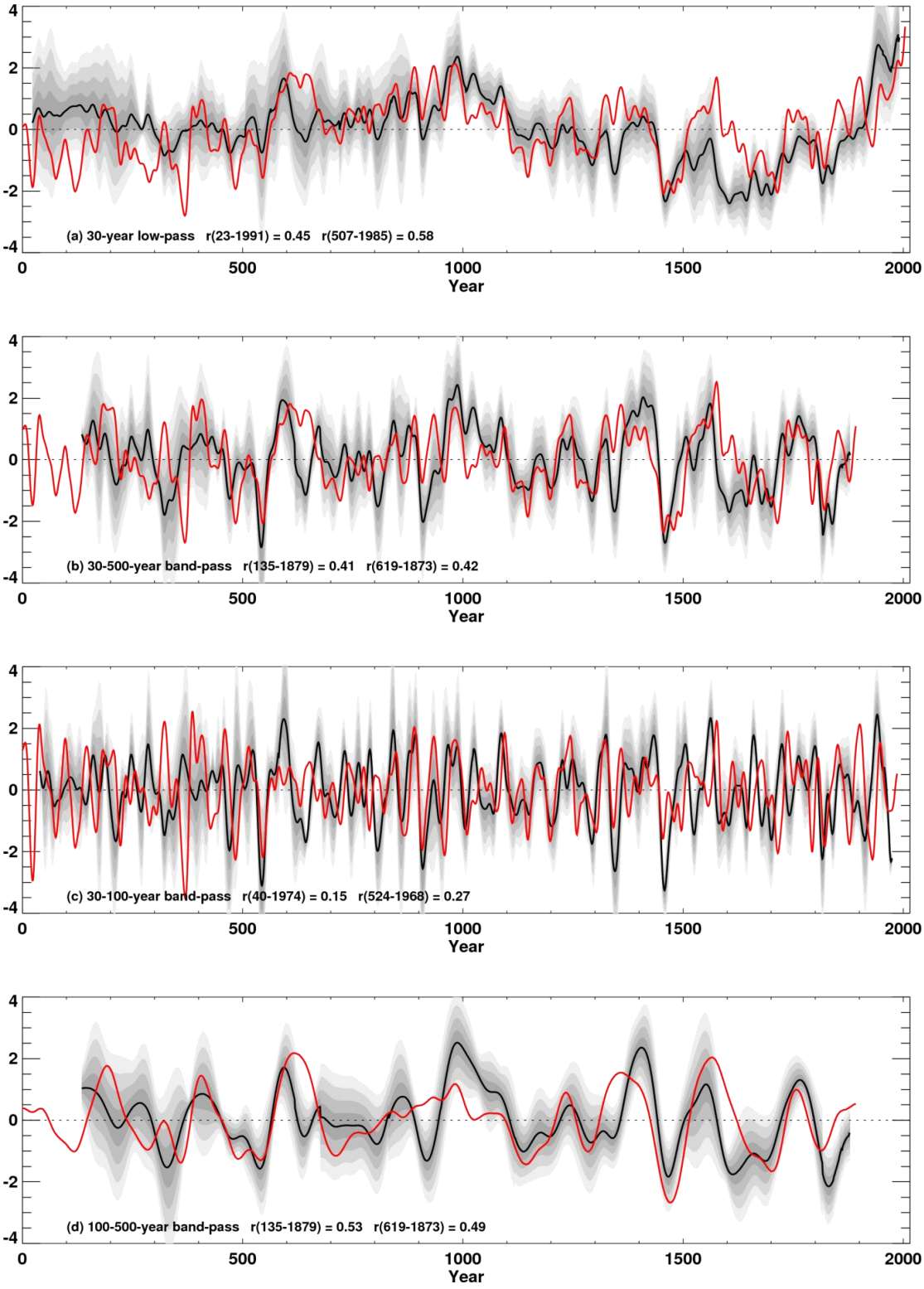

Fig. SG1. Comparison of the QLS chronology (red) and a composite (black) of NH temperature reconstructions using 4 different smoothing filters. See the legend to Fig. 4c in the main paper for further details.

References

1. Melvin TM, et al. (2007) Time-varying-response smoothing. *Dendrochronologia* 25(1): 65-69.
2. Briffa KR, et al. (2013) Reassessing the evidence for tree-growth and inferred temperature change during the Common Era in Yamalia, northwest Siberia. *Quaternary Sci Rev* 72: 83-107.
3. Shao XM, et al. (2009) A 3585-year ring-width dating chronology of Qilian juniper from the northeastern Qinghai-Tibetan Plateau. *IAWA Journal* 30: 379-394.
4. Zhang Y, et al. (2011) Annual precipitation reconstruction since AD 775 based on tree rings from the Qilian Mountains, northwestern China. *Int J Climatol* 31: 371-381.
5. Gou XH, et al. (2010) Tree ring based streamflow reconstruction for the Upper Yellow River over the past 1234 years. *Chinese Sci Bull* 55(36): 4179-4186.
6. Shao XM, Huang L, Liu H, Liang E, Fang X (2005) Reconstruction of precipitation variation from tree rings in recent 1000 years in Delingha, Qinghai. *Sci China Ser D* 48(7): 939-949.
7. Dykoski CA, et al. (2005) A high-resolution, absolute-dated Holocene and deglacial Asian monsoon record from Dongge Cave, China. *Earth Planet Sc Lett* 233(1-2): 71-86.
8. An ZS, et al. (2012) Interplay between the Westerlies and Asian monsoon recorded in Lake Qinghai sediments since 32 ka. *Sci Rep* 2: 619.
9. Mann ME, Lees JM (1996) Robust estimation of background noise and signal detection in climatic time series. Clim Change 33:409-445.
10. Grinsted A, Moore JC, Jevrejeva S (2004) Application of the cross wavelet transform and wavelet coherence to geophysical time series. *Nonlinear Proc Geoph* 11: 561-566.
11. Torrence C, Compo GP (1998) A practical guide to wavelet analysis. *Bull Am Meteorol Soc* 79: 61-78.
12. Steinhilber F, Beer J, Frohlich C (2009) Total solar irradiance during the Holocene. *Geophys Res Lett* 36: L19704.
13. Masson-Delmotte V, et al. (2014) Information from palaeoclimate archives. Chapter 5 in Climate change 2013: the physical science basis. Working Group I contribution to the Fifth Assessment Report of the Intergovernmental Panel on Climate Change (eds. Stocker et al.). In press.
14. Leclercq PW, Oerlemans J (2012) Global and Hemispheric temperature reconstruction from glacier length fluctuations. *Clim Dyn* 38: 1065-1079.
15. Mann ME, et al. (2008) Proxy-based reconstructions of hemispheric and global surface temperature variations over the past two millennia. *Proc Natl Acad Sci USA* 105: 13252-13257.
16. Morice CP, et al. (2012) Quantifying uncertainties in global and regional temperature change using an ensemble of observational estimates: the HadCRUT4 data set. *J Geophys Res* 117: D08101.

17. Jones PD, et al. (2012) Hemispheric and large-scale land-surface air temperature variations: an extensive revision and an update to 2010. *J Geophys Res* 117: D05127.
18. Frank D, Esper J, Cook ER (2007) Adjustment for proxy number and coherence in a large-scale temperature reconstruction. *Geophys Res Lett* 34: L16709.
19. Moberg A, et al. (2005) Highly variable Northern Hemisphere temperatures reconstructed from low- and high-resolution proxy data. *Nature* 433: 613-617.
20. Ljungqvist FC (2010) A new reconstruction of temperature variability in the extra-tropical Northern Hemisphere during the last two millennia. *Geogr Ann A* 92A: 339-351.
21. Juckes MN, et al. (2007) Millennial temperature reconstruction intercomparison and evaluation. *Clim Past* 3: 591-609.
22. Christiansen B, Ljungqvist FC (2012) The extra-tropical Northern Hemisphere temperature in the last two millennia: reconstructions of low-frequency variability. *Clim Past* 8: 765-786.
23. Loehle C, McCulloch JH (2008) Correction to: a 2000-year global temperature reconstruction based on non-tree ring proxies. *Energy & Environment* 19: 93-100.
24. Mann ME, et al. (2009) Global signatures and dynamical origins of the Little Ice Age and Medieval Climate Anomaly. *Science* 326: 1256-1260.
25. Shi F, et al. (2013) Northern hemisphere temperature reconstruction during the last millennium using multiple annual proxies. *Clim Res* 56: 231-244.
26. Ammann CM, Wahl ER (2007) The importance of the geophysical context in statistical evaluations of climate reconstruction procedures. *Clim Change* 85: 71-88.
27. Briffa KR, et al. (2001) Low-frequency temperature variations from a northern tree ring density network. *Geophys Res Lett* 106: 2929-2941.